Tectonophysics xxx (2014) xxx–xxx

Contents lists available at ScienceDirect

Tectonophysics

journal homepage: www.elsevier.com/locate/tecto

Invited Review

Fault slip and earthquake recurrence along strike-slip faults — Contributions of high-resolution geomorphic data

Olaf Zielke [a,*], Yann Klinger [b], J. Ramon Arrowsmith [c]

[a] Department of Earth Science and Engineering, King Abdullah University of Science and Technology, KAUST, Thuwal 23955-6900, Saudi Arabia
[b] Tectonics and Mechanics of the Lithosphere, Institute de Physique du Globe de Paris, IPGP, 75252 Paris Cedex 05, France
[c] School of Earth and Space Exploration, Arizona State University, Tempe, AZ 85287, USA

ARTICLE INFO

Article history:
Received 29 April 2014
Received in revised form 1 November 2014
Accepted 3 November 2014
Available online xxxx

Keywords:
Earthquake recurrence models
High-resolution topography
lidar
strike-slip faults
slip accumulation pattern

ABSTRACT

Understanding earthquake (EQ) recurrence relies on information about the timing and size of past EQ ruptures along a given fault. Knowledge of a fault's rupture history provides valuable information on its potential future behavior, enabling seismic hazard estimates and loss mitigation. Stratigraphic and geomorphic evidence of faulting is used to constrain the recurrence of surface rupturing EQs. Analysis of the latter data sets culminated during the mid-1980s in the formulation of now classical EQ recurrence models, now routinely used to assess seismic hazard. Within the last decade, Light Detection and Ranging (lidar) surveying technology and other high-resolution data sets became increasingly available to tectono-geomorphic studies, promising to contribute to better-informed models of EQ recurrence and slip-accumulation patterns.

After reviewing motivation and background, we outline requirements to successfully reconstruct a fault's offset accumulation pattern from geomorphic evidence. We address sources of uncertainty affecting offset measurement and advocate approaches to minimize them. A number of recent studies focus on single-EQ slip distributions and along-fault slip accumulation patterns. We put them in context with paleoseismic studies along the respective faults by comparing coefficients of variation *CV* for EQ inter-event time and slip-per-event and find that a) single-event offsets vary over a wide range of length-scales and the sources for offset variability differ with length-scale, b) at fault-segment length-scales, single-event offsets are essentially constant, c) along-fault offset accumulation as resolved in the geomorphic record is dominated by essentially same-size, large offset increments, and d) there is generally no one-to-one correlation between the offset accumulation pattern constrained in the geomorphic record and EQ occurrence as identified in the stratigraphic record, revealing the higher resolution and preservation potential of the latter. While slip accumulation along a fault segment may be dominated by repetition of large, nearly constant offset increments, timing of surface-rupture is less regular.

Contents

* Corresponding author.
E-mail address: olaf.zielke@kaust.edu.sa (O. Zielke).

http://dx.doi.org/10.1016/j.tecto.2014.11.004
0040-1951/© 2014 Published by Elsevier B.V.

1. Motivation and Background

One of the fundamental goals of earthquake geology and seismology is to identify earthquake (EQ) recurrence characteristics that enable probabilistic estimates of timing and size of future earthquakes along a given fault (e.g., Burbank and Anderson, 2012; McCalpin, 2009; Stein and Wysession, 2002). While already of distinct scientific interest, the main motivation behind this line of work is to improve assessments of seismic hazard, providing the means to mitigate the eventual destruction that is associated with large earthquakes (e.g., Allen, 2007; Allen et al., 2009; Field et al., 2013). Shedlock and Tanner (1999) reported that 60% of the fatalities from natural hazards are related to catastrophic earthquakes (Allen, 2007). This percentage does not include the devastating earthquakes that occurred within the last 15 years for example in Turkey (1999), India (2002), Iran (2003), Indonesia (2004), Pakistan (2005), China (2008), Haiti (2010), and Japan (2011). Furthermore, many fast-growing megacities are located in seismically hazardous regions. While there has not yet been a large earthquake directly beneath one of these megacities, occurrence of such an event may cause fatalities to exceed 1 million (Bilham, 2004). It is therefore of substantial interest to the public and policy makers to anticipate the type, location, and timing of an earthquake. One approach is to analyze a fault's earthquake rupture history, assuming that this history is a reflection of likely future behavior (Hutton, 1785). Following this assumption, statistical analysis of past EQ record may reveal patterns in EQ recurrence that could be used to make more accurate estimates of the potential timing and size of future EQs. The goal is therefore to reconstruct a fault's EQ rupture history to extract information from that history that enables improved estimates of future behavior of that fault and potentially of faults in general through an improved physical understanding of the rupture process.

While extrapolation of the Gutenberg–Richter relation (Gutenberg and Richter, 1954) may be appropriate to constrain large EQ occurrence probability on a global scale, it is not readily permissible for individual faults or fault sections (e.g., Schwartz and Coppersmith, 1984). Corresponding local-scale magnitude–frequency statistics often consist of a truncated inverse power-law distribution (i.e., the Gutenberg–Richter relation) for small to moderate size earthquakes, and a Gaussian-like distribution of large earthquakes (Fig. 1A; e.g., Ben-Zion, 2008; Wesnousky, 1994). Based on numerical simulations of multi-cycle earthquake rupture, Zielke and Arrowsmith (2008) provide a physical explanation for this bimodal magnitude–frequency distribution. They attribute it to a systematic depth-dependence of constitutive parameters that govern frictional behavior (e.g., Beeler et al., 1994; Blanpied et al., 1991; Dieterich, 1981; Stesky et al., 1974; Tullis, 2007; Tullis and Weeks, 1986) and by that affect down-dip earthquake rupture extent. In this conceptual framework, earthquakes may be grouped into full rupture and partial rupture EQs (FR and PR earthquakes respectively, e.g., Scholz, 1988; Pacheco et al., 1992) where the prior refers to EQs that rupture a fault's full down-dip extent of the seismogenic fault width whereas the latter only ruptures a portion of it (Fig. 1B). In other cases, faults are practically void of small to moderate size seismicity even though occurrence of large EQ ruptures has been historically documented. Small-moderate size event recurrence statistics may therefore not be representative for their larger relatives, thus limiting the value of those instrumental records to constrain large EQ recurrence characteristics.

Alternatively, historical accounts of seismically induced shaking and surface rupture may be used to reconstruct rupture histories (Nur, 2007 and references therein). An ideal historical earthquake record would a) include descriptions that enable constraining EQ size for example through the spatial distribution of shaking intensity levels (e.g., Guidoboni et al., 1994, Toppozada et al., 2002), b) associate the earthquake rupture with specific fault segments, c) give a sufficiently precise EQ age, and d) provide this information consistently through time and over multiple earthquake cycles. In many cases only a few of those requirements are met, distinctly impeding the ability to reconstruct fault rupture patterns from historical accounts (e.g., Nur, 2007).

In the absence of sufficient instrumental or historical records, other data sets are needed in order to determine earthquake recurrence characteristics. Paleoseismology and tectonic geomorphology provide those data sets. Sufficiently large earthquakes may rupture the ground surface

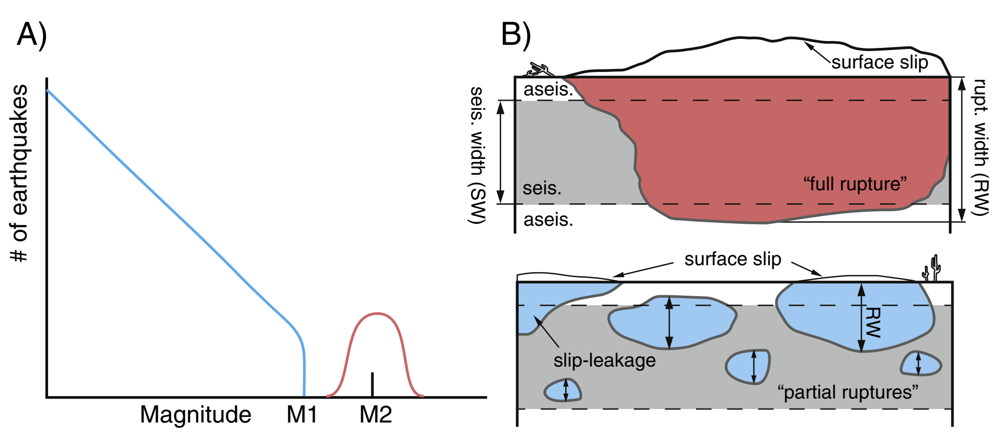

Fig. 1. A) Schematic representation of single-fault magnitude frequency relation (MFR) (e.g., Ben-Zion, 2008; Wesnousky, 1994). While the small to moderate size EQs (magnitude $M < M_1$) form a truncated Gutenberg-Richter (GR) distribution, larger EQs form a Gaussian-like distribution around M_2. EQs with $M < M_1$ may reflect the partial activation of a fault's seismogenic width (SW), whereas the latter (with $M \sim M_2$) reflect the full activation of a fault's seismogenic width (e.g., Pacheco et al., 1992; Scholz, 1988; Zielke and Arrowsmith, 2008). They termed the corresponding EQs to be partial rupture (PR) and full rupture (FR) earthquakes, respectively. B) Schematic representation of the down-dip rupture width (RW) of partial and full rupture EQs along a fault in relation to the extent of SW (e.g., Pacheco et al., 1992; Scholz, 1988; Zielke and Arrowsmith, 2008). While the rupture width of PR earthquakes is always smaller than SW, rupture width of FR earthquakes equals or exceeds SW (King and Wesnousky, 2007). Also shown is an example of slip leakage (Sieh, 1996) where a fault experiences partial rupture due to an EQ along a neighboring fault (segment). Rupture planes are color-coded in correspondence to the portions of the MFR to which they contribute.

(M5.5+; e.g., Bonilla, 1988; Wells and Coppersmith, 1994), forming a range of coseismic features that may be stored in geomorphic and stratigraphic records. Some of them – mainly displaced landforms – can be used to constrain along-fault slip distribution (serving as a proxy for EQ size through EQ scaling relationships; e.g., Wells and Coppersmith, 1994) while disrupted stratigraphic units can be used to bracket EQ timing. Thus, the geomorphic evidence of surface rupture provides valuable information on HOW an earthquake along a given fault is characterized (including rupture extent as well as amount and distribution of fault slip) and whether those characteristics recur (whether portions of a fault that exhibited a certain amount of fault slip in one EQ, exhibited similar slip amounts in other EQs). The stratigraphic evidence provides valuable information on WHEN surface-rupturing events occurred. When combined, stratigraphic and geomorphic records provide information about earthquakes over scales of time and magnitude that are useful for seismic hazard assessment and essential for understanding the long-term rupture patterns of faults (Grant, 2007).

The systematic analysis of displaced geomorphic markers to constrain single-event slip distributions and multi-event slip accumulation patterns of surface-rupturing EQs (Fig. 2A–C) – in other words the fault's surface rupture history – has been introduced almost half a century ago (Wallace, 1968). Much of this early work concentrated on the San Andreas Fault (SAF) system, where climatic conditions relative to deformation rates have been favorable for creating and preserving a multitude of readily observable geomorphic expressions of faulting, including many displaced alluvial features that permit offset measurement. In fact, the south-central SAF exhibits some of the most well preserved tectonic geomorphology at 10s to 1000s of meter scale in the world while at the same time being easily accessible (e.g., Wallace, 1968, 1991). The south-central segment of the SAF last ruptured during the M7.8 Fort Tejon earthquake in January 1857 (e.g., Wallace, 1968), creating a >330 km long surface rupture (Sieh, 1978) with an average fault slip of ~4 m (Zielke et al., 2012). Following the approach outlined by Wallace (1968) and based on conventional field mapping as well as detailed local topographic surveys and air photo interpretation, Sieh (1978) and Sieh and Jahns (1984) reported 150+ geomorphic markers along the 1857 surface rupture trace that were displaced by the most recent and preceding earthquakes. Reconstructions of along-fault slip accumulation based on these measurements were adopted in the formulation of now classical EQ recurrence models (Fig. 2D–F; Schwartz and Coppersmith, 1984; Schwartz and Coppersmith, 1986; Sieh, 1981; Sieh and Jahns, 1984). These seminal contributions (reconstruction of the fault's surface rupture history and its implications for EQ rupture characteristics) have been influential for almost 30 years for seismic hazard analysis and our general understanding of fault behavior.

Reconstructions of along-fault slip accumulation and the derived EQ recurrence models (Fig. 2) are generally non-unique representations of the data set upon which they were built. This non-uniqueness has three main sources: a) constraining a "continuous" along-fault slip distribution from relatively sparse, discrete offset observations presents an underdetermined problem (e.g., Menke, 2012). That is, the number of displaced geomorphic markers is generally too small to enable unique reconstruction results, especially when considering the high offset variability that was documented for recent EQ ruptures (e.g., Elliott et al., 2012; Gold et al., 2013b; Haeussler et al., 2004; Klinger et al., 2006; Mizoguchi et al., 2012; Oskin et al., 2012; Quigley et al., 2010; Rockwell and Klinger, 2013; Rockwell et al., 2002; Toda and Tsutsumi, 2013). b) Complexities and variations in fault geometry and other rupture-controlling parameters directly affect the amount and distribution of coseismic fault slip. Those parameters need to be characterized at high spatial resolution to provide an appropriate framework in which to interpret the acquired offset measurements and identified offset variability. c) Geomorphic markers form and evolve due to the alternation of coseismic slip along a fault and erosional processes operating on the topographic surface. Marker morphology thus reflects not only on the repeating occurrence of slip along a fault but also on the degradational processes that modify its original shape. To properly constrain an earthquake's along-fault slip distribution and subsequently a fault's slip accumulation patterns from displaced geomorphic markers, the initial marker morphology needs to be inferred with confidence and a sound understanding of geomorphic response to prevailing climatic conditions, which alters this initial morphology, is required.

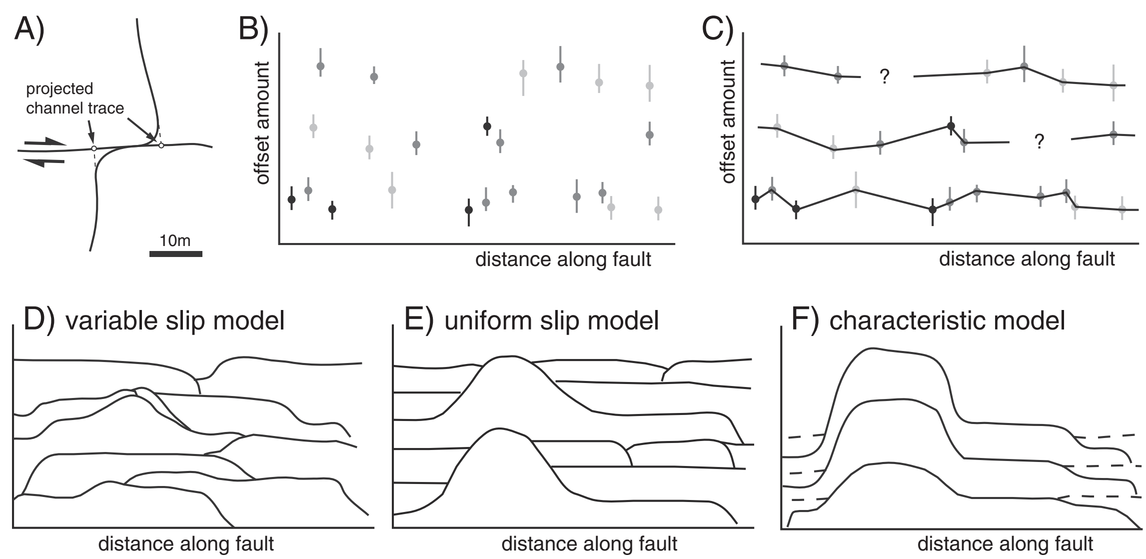

Fig. 2. A–C) Schematic representation of measurement approach and reconstruction of along-fault slip accumulation pattern. A) In the map view, presumably unaltered portions of a disrupted geomorphic marker are projected onto the fault plane, defining the amount of displacement the marker experienced. B) Offset measurements are plotted versus distance along the fault reach. Vertical lines indicate the offset range considered to plausibly reconstruct the displaced feature and colors indicate offset reliability (respective metrics are discussed in detail in Section 3). C) Those measurements may then be used to reconstruct slip distribution of individual events. Depending on offset measurement density such reconstructions will be more or less reliable and unique. D–F) Conceptual models of along-fault slip accumulation and EQ recurrence (Schwartz and Coppersmith, 1984). D) The variable slip model allows earthquakes to occur variably in time and location along the fault. Slip-at-point varies from event to event but satisfies a uniform long-term slip rate. The resulting magnitude–frequency distributions may closely resemble the GR relation. E) The uniform slip model (Sieh, 1981), assumes repeatedly occurring large EQs that have essentially the same slip distribution in each event. Sections of the fault that experience relatively small amounts of slip in those large EQs are considered to rupture frequently in moderate events to catch up with displacement, resulting in a uniform long-term slip rate. Slip-at-point is constant. F) The characteristic EQ model also assumes repeatedly occurring large EQs that have essentially the same slip distribution in each event. Along-fault variations in slip distribution are not filled with "catch-up events" but reflect variations in long-term slip rate along the fault. Slip-at-point is constant.

To address these issues and to validate and possibly improve the existing models of slip accumulation requires high-resolution topographic and imagery data for tectono-geomorphic interpretation, enabling to a) increase the number of offset measurements along a fault, b) analyze its fine-scale fault geometry to provide an appropriate framework for data interpretation, and c) approximate the morphologic response of displaced markers, given the climatic regime they reside in. Technologies that enable acquisition of high-resolution topographic and optical data sets have now become increasingly available. These technologies include terrestrial and airborne light detection and ranging (lidar; Carter et al., 2007; Haddad et al., 2012; Glennie et al., 2013), new generations of satellites for high-resolution optical image acquisition (e.g., Pleiades, http://smsc.cnes.fr/PLEIADES/index.htm; Quickbird and WorldView, www.digitalglobe.com) and DEM-generation from unregistered and uncalibrated optical images via the Structure-from-Motion (SfM) approach (e.g., Fonstad et al., 2013; James and Robson, 2012; Johnson et al., 2014; Westoby et al., 2012). The increasing wealth of high-resolution data sets promises to leave a significant mark on tectono-geomorphic investigations and our view of fault behavior.

Within this review paper, we will begin with a brief discussion of those technologies and corresponding data sets. Then we will discuss the basic requirements to constrain EQ slip from the geomorphic record, followed by an overview of currently adopted measurement strategies. Next we highlight recent investigations of single- and multi-event along-fault slip distributions that utilized the aforementioned high-resolution topographic and optical data sets. We focus our review on ruptures and faults that exhibit dominantly strike-slip motion. In conclusion, we discuss the impact of those recent studies on the current understanding of earthquake recurrence characteristics along strike-slip faults, highlighting a synoptic model for slip-accumulation at fault segment scale which may be understood as a modification of characteristic earthquake model and slip patch model (Schwartz and Coppersmith, 1984; Sieh, 1996).

2. High-resolution data sets for tectono-geomorphic analysis

2.1. Lidar-derived DEM

Lidar-derived DEMs present one type of high-resolution base maps that enable the fine-scale mapping and surveying of fault geometry and displaced geomorphic markers that are needed to further test and improve existing EQ recurrence models. Most of the currently conducted lidar surveys are based on “time-of-flight” ranging (e.g., Bevis et al., 2005; Carter et al., 2007; Glennie et al., 2013; Haddad et al., 2012). The underlying principle is briefly described for airborne lidar surveying (Fig. 3). During data acquisition, a laser scanner emits pulses of monochromatic light. These laser pulses are dispersed and reflected from an object or surface. Reflected pulses that return to the scanner are detected, stopping the time counter which was started when the laser pulse was sent out. The intensity of the returning pulse is recorded along with its time-of-flight. The latter is converted to a distance between scanner (source) and object (reflector), by taking the speed of light through the medium into consideration. This distance is then further converted to provide absolute geographic coordinates for the reflector using onboard inertial navigation system INS for scanner orientation and global positioning system GPS for scanner position. Importantly, each outgoing laser pulse may generate multiple returning pulses that differ in travel time and intensity, for example due to partial pulse reflection by vegetation cover (Fig. 3C). Harding and Berghoff (2000) and Haugerud et al. (2003) for example demonstrated that classification of those returning pulses (e.g., by travel time or curvature-based filtering approaches) enables virtual removal of the vegetation coverage (Fig. 4). The ability to generate high-resolution “bare-earth” DEMs – even for densely vegetated, mountainous, and otherwise inaccessible regions – has become one of the most attractive benefits of airborne lidar and revolutionized geomorphic mapping, particularly in those hard-to-work-in regions (e.g., Barth et al., 2012; Haugerud et al., 2003; Howle et al., 2012; Langridge et al., 2014; Lin et al., 2013; Sherrod et al., 2004). The shot density of a lidar scan (number of pulse returns per unit area) is a function of pulse frequency, distance to target, airplane velocity, and swath overlap. The point clouds, which are generated in the process, may be analyzed directly (e.g., Keller et al., 2010; Nissen et al., 2012; Oskin et al., 2012) or gridded to an equally spaced mesh also known as a digital elevation model (DEM). A common method to identify the appropriate DEM grid-size resolution has been defined by Hu (2003)

$$s = \sqrt{A/n} \tag{1}$$

where s is the estimated grid size, n is the number of sample points and A is the area containing the sample points (Langridge et al., 2014). While the actual value depends largely on flight planning for data acquisition and vegetation coverage, many airborne lidar datasets are sufficiently dense to allow for DEM grid resolutions of ≤ 1 m. More recent lidar surveys with up to 10 returns per m^2 enable grid resolutions as low as ~0.25 m. The same underlying principles of data acquisition generally apply for terrestrial lidar scanning (TLS) and Gold et al. (2012) provide a comprehensive TLS workflow for data acquisition and processing. Respective shot densities (of TLS surveys) are typically two or three orders

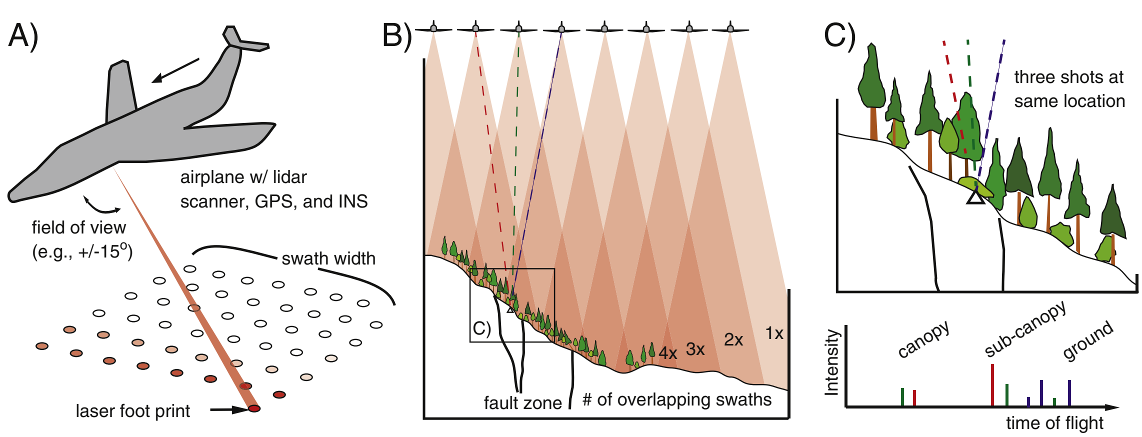

Fig. 3. A) Schematic representation of airborne lidar data acquisition (see also Carter et al., 2007). Swath width is defined by scan angle (field of view) and airplane elevation above ground. Distance between laser footprints (not to scale) defined by shot frequency and airplane velocity (as well as swath width). B) As suggested by Lin et al. (2013), overlap of up to 4 individual swaths is necessary to acquire sufficient ground-returns even in densely vegetated areas (Langridge et al., 2014). C) Example of canopy penetration from different swaths. While “red” and “green” pulses are stuck in canopy or sub-canopy (e.g., by hitting a tree trunk, branches or wide leaves), the “blue” pulse did not exhibit any larger obstacles and made it to the ground surface (as well as back to the scanner). Lower plot illustrates schematically the discrete signal strength from multiple returns some of which ultimately reach the ground.

Please cite this article as: Zielke, O., et al., Fault slip and earthquake recurrence along strike-slip faults — Contributions of high-resolution geomorphic data, Tectonophysics (2014), http://dx.doi.org/10.1016/j.tecto.2014.11.004

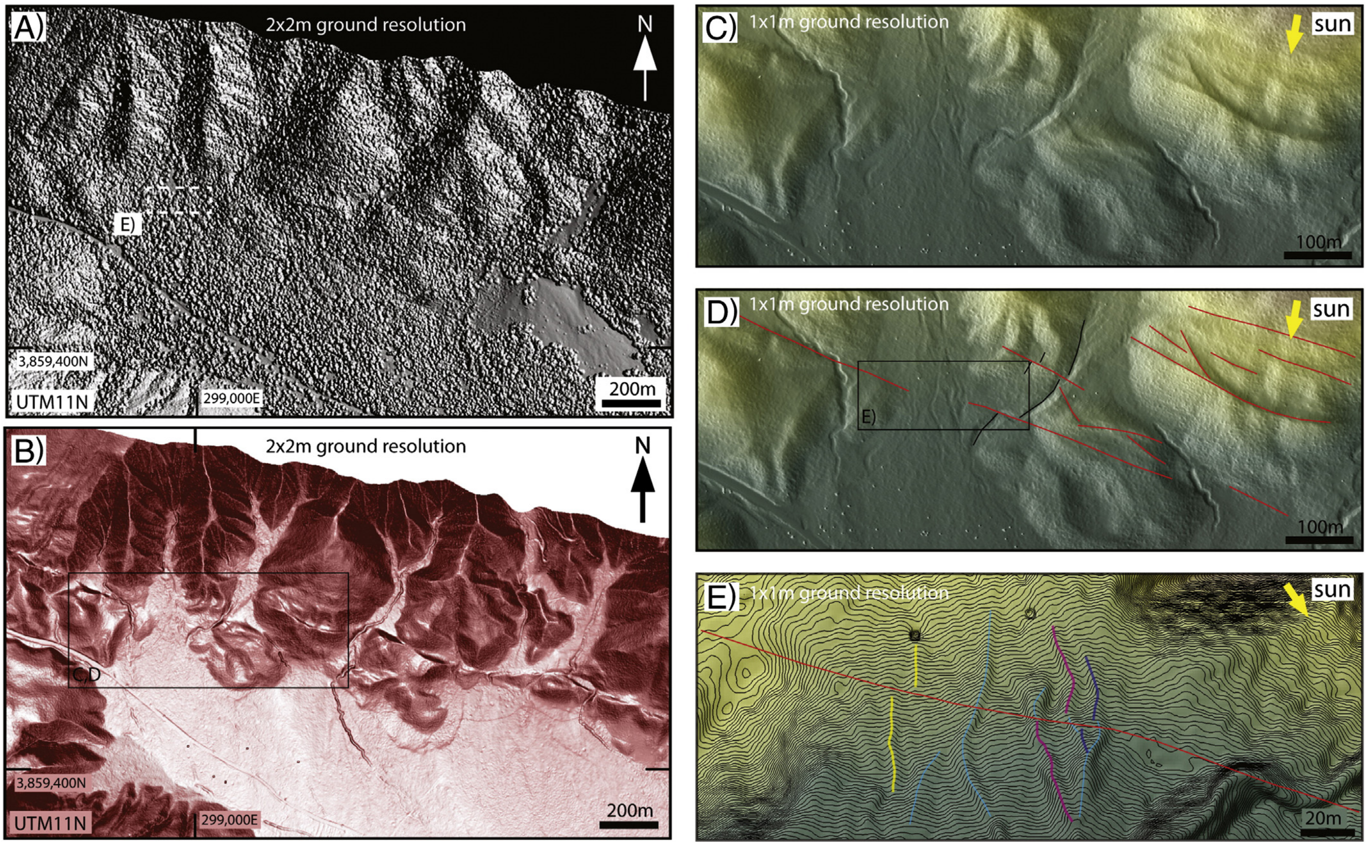

Fig. 4. Portion of the B4 Lidar data set (Bevis et al., 2005) presented to highlight the potential of high-resolution DEM to tectono-geomorphic studies. A) Hillshade plot of first returns (canopy top where present). Only a slight hint of the fault trace is visible. B) RRIM image (combination of slope in red and openness-metric in gray; Chiba et al., 2008), generated from last returns of the same area (using a local minimum approach). Fault traces and displaced landforms are clearly recognizable. C and D) Topo-shade plot of zoomed-in site, with mapped fault zone structure and displaced landforms (indicated by red and black lines respectively). E) Further zoomed-in topo-shade plot combined with 0.2 m contour lines and mapping of fault trace and small gullies (gullies traced in yellow, purple, and dark blue are potentially displaced). While topo-shade and RRIM visualization perform well in fault zone structure identification, addition of contour lines is required to enable detailed tracing of individual gully thalwegs for offset identification. Comparison of A) and E) clearly highlights the strength of Lidar DEM to reveal fine-scale geomorphology even in densely vegetated areas.

of magnitude higher than those from airborne lidar surveys, thus permitting generation of < 10 cm DEM. However, this acquisition approach is limited to local-scale investigations and not suited to survey entire fault systems as is done with airborne lidar for example for the San Andreas Fault system in the B4 project (e.g., Bevis et al., 2005). One goal of this multi-agency project (supported by the National Science Foundation, led by Ohio State University and U.S. Geological Survey, with contributions of National Center for Airborne Laser Mapping (NCALM), UNAVCO, and SCIGN; http://www.earthsciences.osu.edu/b4; Bevis et al., 2005) was to enable studies of past EQ rupture that occurred along the fault system in order to constrain recurrence characteristics. Another goal was to generate a pre-EQ high-resolution topographic data set for comparison with similar data sets acquired after occurrence of the next large rupture. While this event has not yet happened along the SAF itself, pre- and post-EQ lidar data sets have been acquired and differenced for the 2010 El Mayor EQ (Oskin et al., 2012) as well as the 2008 Iwate–Miyagi EQ and the 2011 Fukushima–Hamadoori EQ in Japan (Nissen et al., 2014), revealing a high level of detail in the distribution of single-EQ fault slip and near-fault surface deformation. Conceptually similar differencing approaches also have been introduced for optical imagery (e.g., Klinger et al., 2006; LePrince et al., 2007, 2012; Wei et al., 2011), enabling to constrain single-EQ fault slip and surface deformation for ruptures that were imaged before and after EQ occurrence. An important aspect of the aforementioned B4 project and reason for its ongoing success is that those data are provided to the public domain, for example via data centers like Opentopography (e.g., Crosby et al., 2011; Krishnan et al., 2011; http://www.opentopography.org/index.php) and NCALM (http://ncalm.cive.uh.edu/) and by that contributed for example to numerous tectono-geomorphic research projects (e.g., Arrowsmith and Zielke, 2009; Akçiz et al., 2010; Behr et al., 2010; Gold et al., 2013a; Grant Ludwig et al., 2010; Haddad et al., 2012; Hilley et al., 2010; Madden et al., 2013; Salisbury et al., 2012; Zielke et al., 2010; Zielke and Arrowsmith, 2012; Salisbury et al., subm.). Since acquisition of the B4 data set, many additional lidar data sets have been made publically available through those and other data centers.

Airborne lidar technology is still further advancing in many aspects and Glennie et al. (2013) provide a comprehensive overview on new developments in geodetic imaging by airborne lidar. These developments include a) full waveform lidar, b) multi-spectral lidar, as well as c) the integration of UAV platforms, all of which may soon enable to provide even more informative data sets of surface morphology and composition.

A range of DEM-derived visualizations such as hillshade-, slope-, and contour-plots facilitate fault zone characterization and identification of displaced geomorphic markers. More recently developed visualization approaches further improve the capabilities of those high-resolution DEM for tectono-geomorphic studies. For example, Chiba et al. (2008) developed a "Red Relief Image Map" (RRIM), which combines an "openness" metric of surface concavity (Yokoyama et al., 2002) with topographic slope (Fig. 4B). Visualization of this openness metric resembles hillshade plots, but does not have the potential limitations related to specific illumination angles (Lin et al., 2013; Oskin et al., 2007). Regardless of a feature's orientation, RRIM visualizations always "illuminate" geomorphic features from an angle that highlights their respective topographic expression. In the SOM to this paper, we provide a MATLAB script that enables RRIM generation from lidar-based DEM along with a sample data set.

2.2. High-resolution optical imagery and DEM-derivates

Another data type that is commonly used in tectono-geomorphic investigations is high-resolution optical imagery, which may either be interpreted on its own or be further processed to extract the contained topographic information. Topographic data sets have long been computed from low-elevation stereoscopic airborne photos as part of the routine process by mapping agencies all over the world. Severe restrictions, however, often impeded access to such kind of data in many countries, based on national security reasons. Indeed, it often stopped the earth science community to access high-resolution DEM needed to perform detailed geomorphological studies. In the last ten years, a new generation of high-resolution optical satellites has been launched —including the Quickbird, WorldView, and Pleiades platforms (www.digitalglobe.com; http://smsc.cnes.fr/PLEIADES/) with sub-meter ground resolutions as low as ~0.3 m. High-resolution optical imagery has become available for practically any place on the planet and a number of commercial and open-source software packages for image correlation were developed, enabling to constrain along-fault slip distribution and surface deformation for recent earthquakes (e.g., Klinger et al., 2005; LePrince et al., 2007; Rosu et al., 2014). In addition to better ground resolutions, the new sensors usually have also a better image depth that allows for improved discrimination of natural features used to recognize, for example, past earthquake offset features (Klinger et al., 2011). Several of these newly-launched satellites are equipped with highly agile sensors, allowing for multi-scopic acquisitions of the same scene during a single satellite pass to avoid any issue related to diachronism between successive images. These new technological developments also allow for DEM computation with sub-meter ground resolution from those optical satellite images without shadow zones, even in areas with steep topography.

High-resolution DEMs may also be generated via the "structure-from-motion" (SfM) approach (e.g., Brown and Lowe, 2005; Dellart et al., 2000; Hartley and Zisserman, 2004; Lowe, 2004; Triggs et al., 1999) from a large number of photographs that image an area of interest from many different viewpoints. SfM is much simpler from the users' perspective and also much less expensive than traditional photogrammetry because camera parameters as well as camera location and orientation are calculated automatically using information generated directly from the images. DEM accuracy and processing time further improve if camera calibration and position are known. Modern small and lightweight digital cameras provide sufficiently high resolutions for the SfM approach and may be mounted on kites, balloons, or other UAVs. Thus, the combination of SfM approach with airborne systems provides a powerful alternative to other site- and local-scale high-resolution DEM generation approaches (e.g., Fonstad et al., 2013; James and Robson, 2012; Johnson et al., 2014; Westoby et al., 2012).

3. Offset quantification and documentation

In this section, we will discuss the requirements to make meaningful offset measurements and suggest some guidelines for measurement approach and documentation. Those requirements a) ensure causal relationship between two separated geomorphic marker sections, b) confidently infer the pre-EQ morphology of the separated marker sections, and c) ensure that marker production rate is generally higher than the occurrence of surface rupturing EQs. While the concepts outlined here apply to geomorphic markers in general, we concentrate on fluvial and alluvial features within an environment that is dominated by strike-slip motion.

3.1. Matching markers and pre-EQ morphology

Landforms, linear trends, and discrete lithological contrasts that continued across the fault prior to an earthquake and for which the pre-deformation geometry can be inferred with sufficient confidence provide the means to measure offsets and by that constrain fault slip (e.g., Cowgill, 2007; Burbank and Anderson, 2012; McCalpin, 2009). In order to measure the offset of a geomorphic marker, the corresponding marker sections must have been connected across the fault zone in a continuous way. As is indicated in the examples in Figs. 5 and A1 (in SOM) which focus on displaced fluvial features, ensuring this causal relation between marker sections is not always simple or even possible. Relative size and curvature of respective marker sections, their current geomorphic expression (i.e., how "fresh" respective marker sections appear), and the climatic/geomorphic framework in which the feature resides provide valuable information to gain the required confidence. Apparently displaced geomorphic features for which a causal relation cannot be ensured should not be used to measure earthquake surface slip (Fig. 5).

Once the causal relationship between geomorphic marker sections and the fault trace can be ensured, it is further required to infer their pre-EQ morphology with sufficient confidence. By that we largely refer to the appropriate projection of up-fault and down-fault marker piercing lines onto an idealized single and locally linear fault trace (Fig. 6). Even if up-fault and down-fault marker sections are part of the same geomorphic feature, it may be difficult or not possible to confidently estimate the pre-EQ morphology — depending on marker dimension and orientation, as well as the extent of the overprinted area around the fault in which the pre-EQ morphology has been modified by the combination of tectonic and erosional forces (Fig. 6). This is of distinct importance because the measured offset amount is a direct outcome of the assumptions of pre-EQ morphology and its projection onto an idealized fault plane. An offset measurement is only as good and meaningful as the estimate of the pre-EQ marker morphology and fault trace orientation. The level to which they can be constrained should be reflected in the uncertainty quantification, associated with offset measurements that are taken.

3.2. Marker formation vs. marker displacement

Utilizing the geomorphic record to constrain the rupture history along a fault is based on a fundamental assumption: the production rate of geomorphic markers that is used to measure displacement is assumed to be (distinctly) greater than the recurrence rate of (surface-rupturing) earthquakes. As a consequence of this assumption, a suite of landforms is built between successive earthquakes. Those suites of landforms are offset en masse in the following earthquakes, generating groups of offsets along a fault section where the smallest local offset represents fault slip of the MRE (Fig. 7; e.g., Klinger et al., 2011; Madden et al., 2013; McGill and Sieh, 1991; Sieh and Jahns, 1984; Sieh, 1978; Wallace, 1968; Zielke et al., 2010; Zielke et al., 2012). Clusters of geomorphic offsets identified along a certain fault section represent fault slip from the same event. Clusters of offsets with different mean values (identified along the same fault section) would thus represent cumulative slip amount from different numbers of events (Fig. 7). If this fundamental assumption is not met and earthquakes would occur more frequently than the formation of geomorphic features, then some of those (frequently occurring) earthquakes may not be resolved in the geomorphic record (although they may still be identified in the stratigraphic record), limiting the reconstruction of slip-per-event and slip accumulation pattern.

Burbank and Anderson (2012) point out that each earthquake that is sufficiently large to modify the hydrologic and geomorphic conditions may also increase susceptibility to erosion and by that increase marker production rate for some time after large EQ occurrence. Thus, large EQs could promote formation of new geomorphic markers at corresponding

Please cite this article as: Zielke, O., et al., Fault slip and earthquake recurrence along strike-slip faults — Contributions of high-resolution geomorphic data, Tectonophysics (2014), http://dx.doi.org/10.1016/j.tecto.2014.11.004

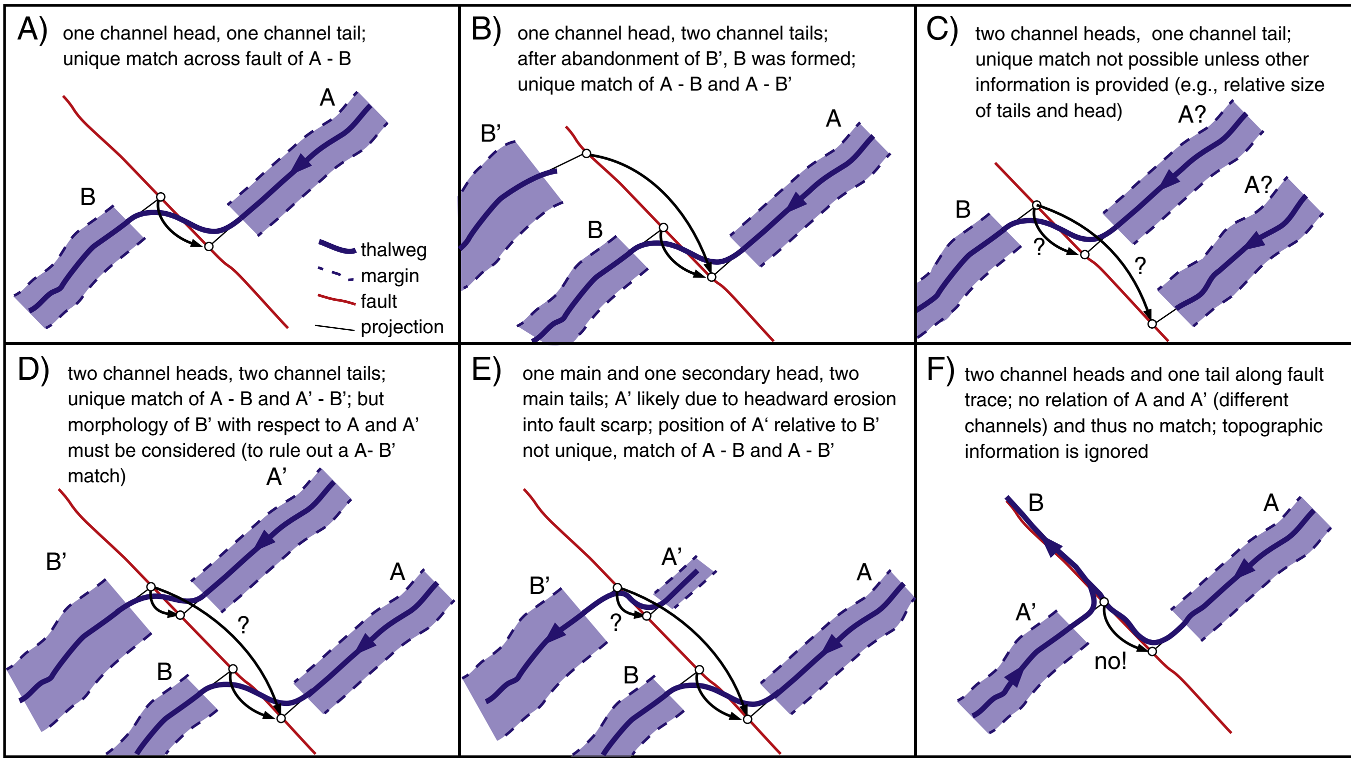

Fig. 5. Schematic representations of commonly observed relations between horizontally displaced features (e.g., small fluvial channels) and fault trace to highlight the potential difficulties in identifying whether individual marker sections were originally connected or not. Head and tail nomenclature are from Lienkaemper (2001). Question marks indicate questionable reconstructions in which a causal relation between both marker sections cannot be ensured. Each displaced feature must be carefully studied to ensure an original connection between observed up-fault and down-fault marker sections.

spatial scales in subsequent storm events, enabling to resolve slip-distribution of the following EQ in detail. Smaller surface-rupturing EQs on the other hand disturb the morphology in a less severe way and therefore provide less ready opportunities to form new markers in subsequent storm events. In those latter cases, the severity and spatial extent of regional-scale weather events – the second major control on marker formation – might be the factor that dominates the formation of new geomorphic features (as opposed to afore-mentioned potential control of large-scale EQs on morphological susceptibility for new channel formation). It is important to understand that the severity of those weather events is inversely proportional to their recurrence frequency and much like global seismicity following an inverse-power law relationship (e.g., Bruce, 1968; Hershfield, 1961; Madsen et al., 2009; Miller, 1963). The number and spatial distribution of newly formed geomorphic features hence differs for storm events that recur on decadal and centennial time scales as much as it differs in response to moderate and large surface-rupturing EQs that potentially modified erosional susceptibility (Burbank and Anderson, 2012).

Sieh (1978) identified dozens of fresh or rejuvenated geomorphic markers, exhibiting apparently no displacement as they cross the south-central SAF that most recently generated surface rupture in 1857 (the aforementioned M7.8 Fort Tejon EQ). Those markers presumably formed after this most recent rupture, some of which demonstrably during the mid-1970s when Sieh (1978) conducted his field work. This observation is of importance as it highlights that geomorphic and hydrologic conditions in this area are sufficiently dynamic and morphological susceptibility for new channel formation is sufficiently high to cause frequent marker production over the century after the earthquake. Assuming that the amount of newly formed geomorphic markers is representative for inter-event marker production along the south-central SAF, Sieh (1978) concluded that marker production rate exceeds marker displacement rate, therefore complying with the mentioned fundamental requirement. He suggested that marker production recurs on a decadal time scale (potentially linked to ENSO events which generally cause higher precipitation in south-central California; e.g., Schonher and Nicholson, 1989) whereas surface displacement recurs on a centennial time scale, so that a multitude of markers would form between events, differentiating fault slip contributions from successive EQs. But can this suggested (relative) marker production rate be translated to other regions, for example in different (non-arid) climatic conditions? We suggest that the question of relative frequency of marker production and displacement must be addressed individually for each fault system, to test whether the approach (constraining single-event slip from measuring displaced geomorphic markers) is appropriate. While not frequently done, we advocate providing not only records of displaced geomorphic markers, but also those that are not displaced and thus are presumably younger or rejuvenated. This gives some general understanding on relative marker production rate and overall system dynamics.

3.3. Offset measurement and uncertainties

If those above-mentioned fundamental requirements are met, then the slip accumulation pattern along a fault can be constrained via the geomorphic record (e.g., Beauprêtre et al., 2012; Madden et al., 2013; McGill and Sieh, 1991; Salisbury et al., 2012; Schwartz and Coppersmith, 1984; Sieh, 1978; Sieh, 1996; Sieh and Jahns, 1984; Wallace, 1968; Zielke and Arrowsmith, 2012). The first step is to carefully map the geomorphology of the fault zone to identify rupture trace(s) and their potential complexities. This provides the framework in which to interpret offset values of identified displaced markers, for example distinct changes in observed offset amount in an area of fault geometric complexity (e.g. step-over; fault bend). When the fault trace is identified, displaced geomorphic markers may be located along those traces. As mentioned before, focus must lie here on ensuring a causal relation between geomorphic marker sections (i.e. that they

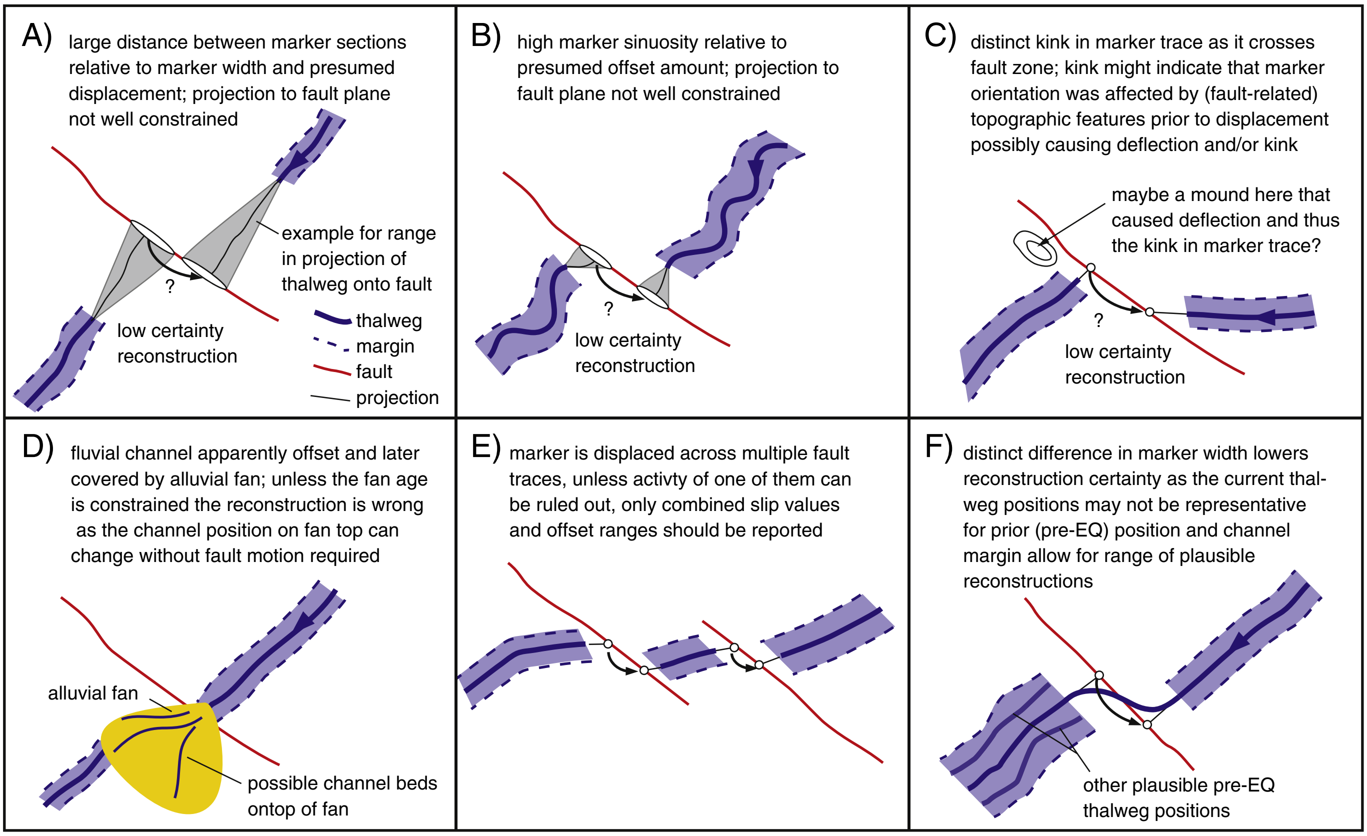

Fig. 6. Schematic representation of scenarios for which the estimation of pre-EQ morphology is impeded. Much of the corresponding uncertainty relates to difficulties in confidently projecting what is assumed to be the unaltered pre-EQ marker morphology. The actual width of the fault zone (approximated as a single fault plane for the purpose of marker projection and offset measurement), along which shearing and geomorphic modification may severely change the initial marker morphology, further contributes to those uncertainties. Gray areas outline the projection range. In many cases, it is better to aim to fit not only the thalweg position but rather the overall shape of the channel (including channel margins and riser all at the same time).

have been originally connected) and the ability to assess the pre-EQ morphology (Figs. 5 and 6). The identification of fault trace and displaced features should incorporate the whole range of available data, including tectono-geomorphic interpretations of field observations and optical imagery, and a wider spectrum of DEM-derivatives such as hillshade-, RRIM-, and contour maps to ensure acquiring the most complete understanding of the site morphology possible. Feature identification for example works well with hillshade-, RRIM-, or slope-shade visualizations. The actual offset measurement however is often better done by further including contour maps, which enables a more precise tracing of marker shape and its projection onto the fault trace. Field observations and optical imagery provide valuable means to check the remotely acquired results.

Different measurement approaches have been used to quantify the offset of tectonically displaced geomorphic markers, largely depending on available data set and analysis tools (e.g., Beauprćtre et al., 2012; Gold et al., 2013a; Klinger et al., 2005, 2006, 2011; McGill and Sieh, 1991; Rockwell and Klinger, 2013; Salisbury et al., 2012; Scharer et al., 2014a; Sieh, 1978; Zielke et al., 2012). Those approaches range from tape measurements in the field to back-slipping (i.e., retro-deforming) displaced markers to the assumed original shape using high-resolution aerial photography/satellite or DEM data. Another approach using DEM data is to cross-correlate cross-sectional profiles of up-fault and down-fault marker sections that are projected onto an idealized fault plane (e.g., Hudnut et al., 2002; Zielke and Arrowsmith, 2012). The goal of those different approaches is the same: to find the offset that most likely represents the "true" fault slip value and further assign appropriate uncertainty bounds to it.

Two metrics for uncertainty are commonly attributed (e.g., Sieh, 1978; Weldon et al., 1996; Klinger et al., 2011; Zielke and Arrowsmith, 2012; Scharer et al., 2014a; Salisbury, et al., subm.). The first is a confidence measure, qualitatively describing how well the pre-EQ morphology can be approximated and whether the observed separation between two marker sections is considered to be of tectonic origin. It thus reflects on the relation between observed separation and actual fault rupture behavior and how reliable our assumption of the pre-EQ marker morphology is (Figs. 5 and 6). Typically, qualitative descriptions for offset reliability such as "high", "moderate", and "low" are assigned. It can be considered an epistemic uncertainty, reflecting our lack of knowledge of the actual shape of the feature before disruption and its morphological modification since then.

The second uncertainty measure quantifies the range of offset values that are capable of restoring the assumed pre-EQ marker morphology sufficiently well. This range (e.g., +/− 1.4 m) represents the physically plausible offset range (typically considered to represent 2σ) (e.g., Klinger et al., 2011; McGill and Sieh, 1991; Scharer et al., 2014a; Zielke et al., 2012). This quantitative uncertainty metric (aleatoric) is thus very much linked to the fact that geomorphic markers as well as the fault zone are not "lines" but have a spatial extent. The assigned offset range is further linked to the ground-resolution of the utilized data set (e.g., DEM resolution of 0.5 m), which provides its lower bound. Proper indication of the offset range, its quality, and its relation to 1 or 2σ uncertainty facilitates further processing steps such as the computation of a coefficient of variation *CV* (e.g., Biasi, 2013; Goes and Ward, 1994; Hecker et al., 2013; Scharer, 2013; see below).

Practically, we would first use for example slope-shade or topo-shade visualizations of the DEM – as well as field observation and tectono-geomorphic interpretations of optical imagery when available — to identify the fault trace and search for potentially displaced markers (Fig. 8). We inspect the site's geomorphology in

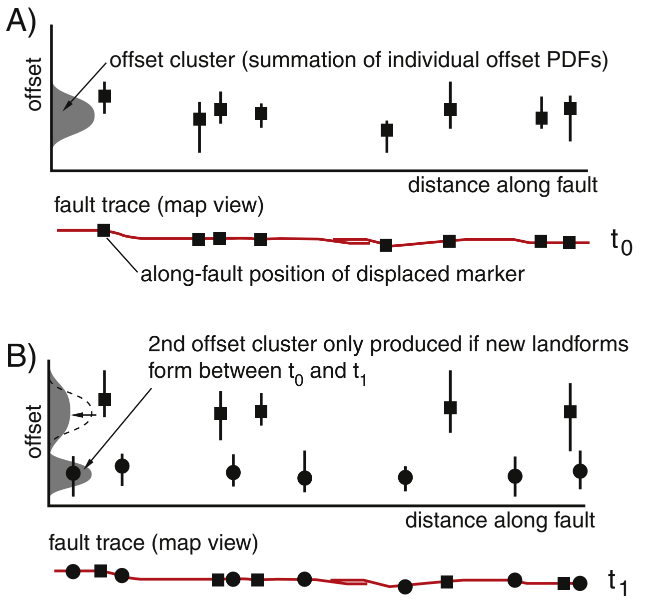

Fig. 7. Representation of marker production rate relative to marker displacement. A) Assume an EQ occurs at t0. Prior to that EQ, a number of undeformed landforms existed, crossing the fault zone (squares along fault trace). At time t0 those landforms were displaced en masse. Measurements of those offsets may be combined (summation of individual offset PDFs) to form an offset cluster (*COPD*, see text). B) At time t1 another EQ occurs. If markers formed between t0 and t1, those markers (circles along fault trace) would also be displaced en masse as well, forming a second offset cluster. At the same time the previously displaced landforms would also be displaced during the t1 EQ, shifting the first offset cluster to higher displacement amounts. Because geomorphic markers will be modified and/or obliterated by degradational processes, offset clusters for larger slip amounts are generally wider and have smaller amplitudes. If on the other hand no landforms were formed between t0 and t1, then the second offset cluster would not exist while the first would still shift to higher displacements. The resulting offset cluster would contain slip of more than one EQ, limiting the capabilities to distinguish the slip-per-event and to reconstruct the single-event slip accumulation pattern.

detail, including contour maps, for example to assess likelihood of channel deflection (as opposed to tectonic displacement). Next, we trace the idealized fault plane as well as the portions of up-fault and down-fault marker section that are considered to still represent the initial pre-EQ morphology (preferentially by incorporating contour maps). Taking the trace of those markers and their distance to the fault trace into account, we project those sections with pre-EQ morphology onto the fault plane (Fig. 8) to determine the offset. This processing step benefits from analysis of remotely sensed data (as opposed to field observations) as one can easily view the entire length of an offset feature at nearly uniform scale, whereas a ground observer standing on the fault observes in detail only the few meters of the feature nearest the fault which may exhibit severe degradational overprinting (Lienkaemper, 2001; Oskin et al., 2007). Depending on marker morphology (e.g., size, curvature, thalweg width) and fault geometric complexity, we would assign a qualitative rating to this offset measurement. Then, assuming that this marker projection IS valid (as the corresponding uncertainty is already incorporated via the qualitative metric), we determine the offset range that is capable of reconstructing this assumed pre-EQ morphology sufficiently well. Depending on measurement approach, those offset ranges are assigned in different ways (e.g., Brooks et al., 2013; Gold et al.,2013b; Madden et al., 2013; McGill and Rubin, 1999; McGill and Sieh, 1991; Salisbury et al., 2012; Scharer et al., 2014a; Zielke et al., 2010, 2012) for example via retro-fitting the surface morphology, repeated offset measurements, or measuring offsets of different portions of the same marker (e.g., measuring thalweg displacement as well as displacement of both channel edges). Each offset value within this range has a probability assigned to it, reflecting on the likelihood that it represents the "true" slip fault slip value (e.g., McGill and Sieh, 1991). Thus, regardless of the shape of those ranges (e.g., box-car, triangle, truncated Gaussian), they represent probability density functions (PDFs) that constrain the physically plausible offset range. The PDF area (or height) can be scaled to account for the relative quality of the feature.

As becomes clear, a main source of measurement uncertainty is related to the correct identification of fault trace position and orientation in relation to marker position and orientation as well as the proper assessment of the pre-earthquake marker morphology for projection onto the fault trace. The level to which a measured separation relates to actual offset (i.e., fault slip) hinges on correctly identifying those tectono-geomorphic parameters. Retro-deforming the surface is an important step in assessing how well a certain offset amount is capable of reconstructing the assumed pre-EQ morphology (Fig. 8D).

Another source of uncertainty relates to the interpreter. Offset measurements can be biased. As was noted by Weldon et al. (1996): "This bias could be derived from the unconscious choice of a best match of uncertain features that is consistent with previous choices. This statement is not meant to suggest any impropriety in the data collection, but to acknowledge that it is extremely difficult to avoid bias where measurements of "matches" involves interpretation of the exact location of the features being measured. From experience we know that after one finds several convincing offsets, one's eye is keyed to looking for matches in that range, so that one will often overlook or misinterpret offset that are unexpected, thus biasing the sample". As a way to minimize the potential for measurement bias, we propose to adopt a "blind measurement" approach. Depending on available data set, blind measurement can be more or less easily implemented. The general measurement approach would remain the same as was just described (for example measuring offsets with tape measure in the field, back-slipping air-photo or DEM data set to restore a displaced feature, cross-correlation of cross-sectional profiles that are projected onto the fault plane). However, offsets will be measured in units that are unknown to the person measuring. Those units should be defined randomly and changed from measurement to measurement. In terms of measuring offsets in the field, one could envision a set of custom-made tape measures with different unit lengths. The interpreter will perform the analysis as always, noting the determined "offset amount" as well as the tape measure that was used to measure it. The interpreter gets to see the actual displacement value (converting the arbitrary units to meters for example) only after (all) the measurements are completed. Implementing blind measurements is particularly simple when measuring displacements on a computer with corresponding software such as LaDiCaoz (e.g., Zielke and Arrowsmith, 2012). Zielke has recently upgraded this MATLAB-based GUI for measuring and back-slipping displaced geomorphic features (LaDiCaoz_v2) to include this blind measurement approach (https://sites.google.com/site/olafzielkephd/matlab-scripts). He also provides an equivalent tool (MATLAB-based GUI) for blind measurements on optical imagery that is based on a retro-fitting approach (also available on this website). Repeated blind measurements, conducted at different times will further minimize bias, thus improving a study's reliability.

A number of recent studies further addressed the repeatability of offset measurements and respective challenges in consistently measuring small geomorphic offsets (e.g., Zielke and Arrowsmith, 2012; Scharer et al., 2014a; Salisbury et al., subm.). For that, a group of users with varying experience level in tectono-geomorphic interpretation was asked to measure the offset of a number of displaced geomorphic features remotely using different measurement approaches (e.g., paper image and scale, Google Earth ruler tool, MATLAB-GUI LaDiCaoz) or in the field. For all survey methods, the majority of responses are in close agreement. However, large discrepancies arise where users interpret landforms differently — specifically the pre-earthquake morphology, total offset accumulation, and degradational evolution of offset geomorphic features. Experienced users make more consistent measurements, whereas beginners less-consistently choose the same interpretation for an offset feature (Salisbury et al., subm.). Scharer et al. (2014a)

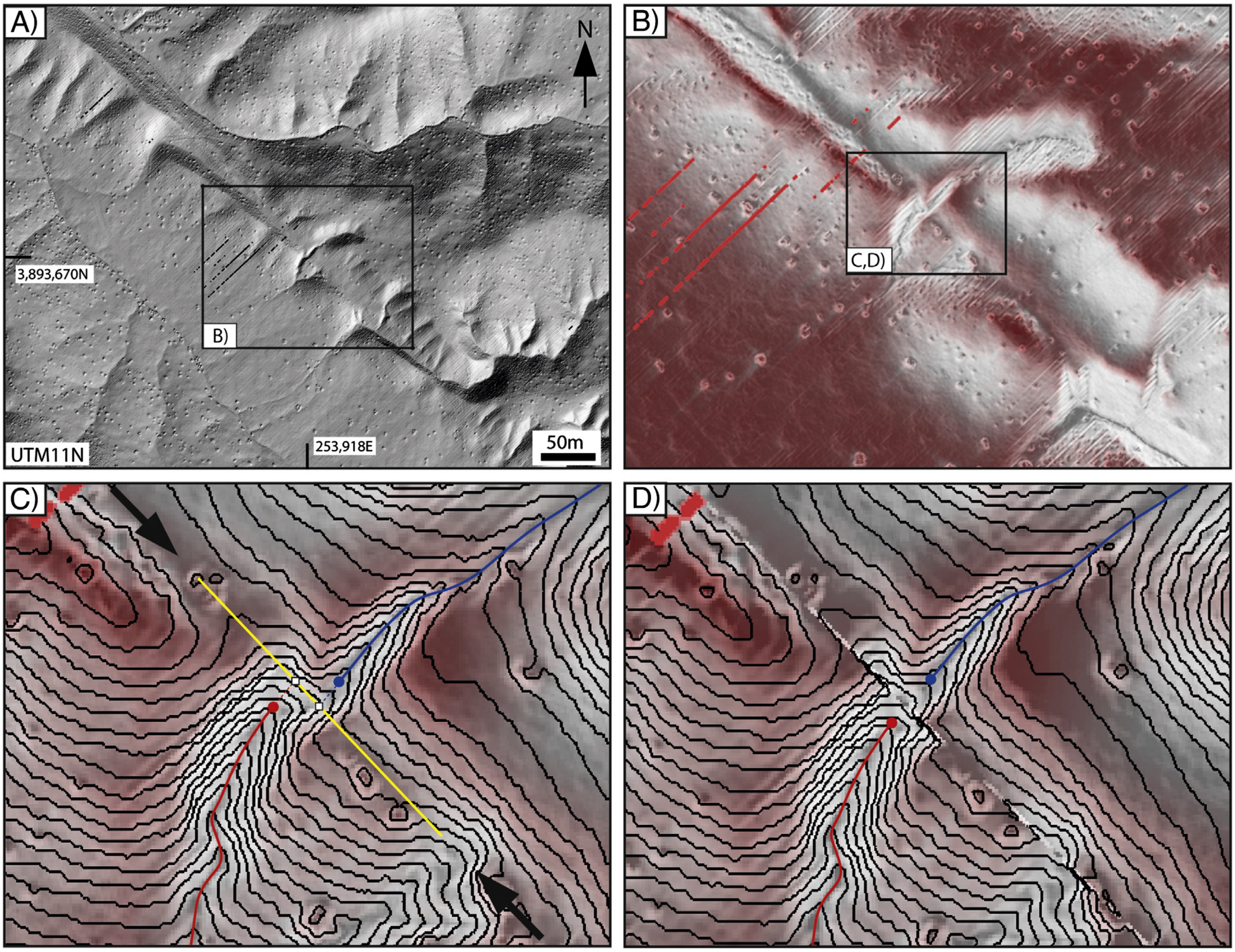

Fig. 8. Representation of an offset measurement, using a 0.5 m grid resolution airborne lidar data set. A) The fault trace is examined for potentially displaced geomorphic markers. B) A close-up of the potentially displaced features indicates the site's tectonic geomorphology. C) Displaced marker sections are traced (red and blue lines along channel thalweg) and projected onto an idealized planar fault (indicted by white squares along the fault trace yellow line). Contour plots facilitate this analysis step. D) The landscape is retro-deformed by the determined offset amount to assess reconstruction reliability and offset range.

recommended that field mapping should be combined with analysis of high-resolution topographic data and optical imagery – supplemented with subsurface investigations when critical – to gain the most complete understanding of the site's morphology and by that enable more consistent offset measurements.

Modern data storage opportunities/capabilities for digital data such as high-resolution imagery and DEM provide the means to publish not only interpreted results, but the full underlying data basis as well, as was done for example by Zielke et al. (2010, 2012). Doing so enables other researchers to validate the respective work, increasing transparency and overall reliability of the respective investigations. We advocate to use the existing storage options provided by publishers, universities, and other agencies to give future researchers access to uninterpreted as well as interpreted data.

4. Recent studies

A number of recent studies have used high-resolution topographic data sets and imagery to constrain the along-fault slip distribution of recent ruptures as well as the accumulation of slip due to occurrence of multiple earthquakes. In the following, we highlight some of those results and put them into context with previous studies on single-event surface slip distributions and along-fault slip accumulation patterns.

4.1. Single-event slip distribution

Before investigating accumulation patterns of slip, the first step is to investigate the fault slip distribution of the most recent earthquake (MRE). Those single-event investigations – eventually serving as templates to analyze and reconstruct multi-event slip accumulation patterns – emphasize ruptures of the last few decades, imaged or surveyed quickly after the event occurred. In those cases, geomorphic overprinting of fault zone and displaced features is negligible and even small-scale geomorphic or anthropogenic markers and their pre-EQ morphology can be identified and measured. Because erosion of rupture features is still minor, the potential shortcomings of field-based offset observations (Lienkaemper, 2001) are less relevant and along-fault slip distributions of recent ruptures are usually derived from field measurements (e.g., Akyüz et al., 2002; Haeussler et al., 2004; Klinger et al., 2005; Mizoguchi et al., 2012; Quigley et al., 2010; Sieh et al., 1993; Toda and Tsutsumi, 2013; Xu et al., 2006; Zachariesen and Sieh, 1995) or optical imagery (Rockwell and Klinger, 2013). This approach is increasingly complemented by studies that enable to determine along-fault slip and surface deformation from lidar-differencing and image correlation techniques (e.g., Klinger et al., 2005; LePrince et al., 2007; Nissen et al., 2014; Oskin et al., 2012).

Practically all investigations of single-event fault slip distributions have identified distinct along-fault variations in surface slip that span a range of spatial scales. Following the M7.2 2010 El Mayor EQ, Gold et al. (2013b) conducted a very high-resolution terrestrial lidar survey (TLS) survey with shot densities exceeding 10^3 points/m^2 along three ~200 m long sections of the earthquake's ~120 km surface rupture. They identified numerous offset features and measured them multiple times to assess along-fault offset variability and measurement uncertainty. For two of those sections, a mean offset of 2–3 m was reported. Individual offset measurements deviated from their respective mean by up to 11% (representing 2σ), resulting in an offset range of ca. +/− 25 cm (Fig. 9A). Mean offset at the third section – which is structurally more complex than sites 1 and 2 – was ~1.5 m, exhibiting up to 17% deviation from the mean (i.e., a +/− 25 cm offset range). Gold et al. (2013b) show that the identified offset ranges are directly related to the ability to consistently project displaced geomorphic features onto the idealized fault plane. This in turn is further related to the geomorphic characteristics of the displaced feature (e.g., feature sharpness — the topographic curvature at length-scales similar to the offset amount) as well as the actual width of the fault zone (which is approximated as a single fault plane). The high relative amount of this aleatoric uncertainty (~11–17% deviation from offset mean) highlights that constraining the geometrical configuration of fault plane and displaced markers is not trivial, even for very young and pristine features that were surveyed at very high spatial resolution only days after the causative EQ.

Rockwell and Klinger (2013) analyzed a 15 km long section of high-resolution air photos (1:7200 scale) that were taken soon after the M7.1 Imperial Valley EQ generated a ~60 km long surface rupture in 1940 (e.g., Sieh, 1996), to constrain the along-fault surface slip distribution. Almost 650 measurements were made, largely based on displaced cultural features such as rows of crops and trees with well known pre-EQ across-fault extension, presumably resolving offsets at ~0.1 m precision (Rockwell and Klinger, 2013). The surface rupture of this event features two sections, exhibiting distinctly different amounts of mean slip and a high slip gradient between those sections (Fig. 9B). Slip along both sections was localized in a very narrow fault zone (<10 m wide). While the southern section had an average slip of 5.5 m, slip along its northern counterpart was distinctly lower, averaging only ~1 m and suggesting distinct differences in rupture controlling parameters along respective sections. Measured offsets within each section varied by up to 30% of the respective segment mean in an apparently random manner at < = 100 m length-scales (Fig. 9B). This kind of apparently random variability of slip was identified in practically all investigations that surveyed the along-fault slip distribution at appropriate (sub-km) spatial resolution including the 1992 Landers EQ (McGill and Rubin, 1999; Zachariesen and Sieh, 1995), the 1999 Izmit EQ (Rockwell et al., 2002), the 2002 Denali EQ (Haeussler et al., 2004; Schwartz et al., 2012), the 2010 El Mayor EQ (e.g., Gold et al., 2013b; Oskin et al., 2012), the 2010 Darfield EQ (Elliott et al., 2012; Quigley et al., 2010), and the 2011 Fukushima–Hamadoori EQ (Mizoguchi et al., 2012; Nissen et al., 2014; Toda and Tsutsumi, 2013). While aleatoric contributions to this uncertainty range can be assumed (presumably contributing a minimum of 10–15% to this variation), the documented high offset variability (30%) suggests existence of an additional, epistemic uncertainty component. Considering the spatial scales at which this variability is observed (offset changing by a meter or more within a few 10s to 100 s of meters along the fault), those epistemic components must have a source that is located at very shallow depths and is possibly attributable to the non-elastic (and non-linear) response

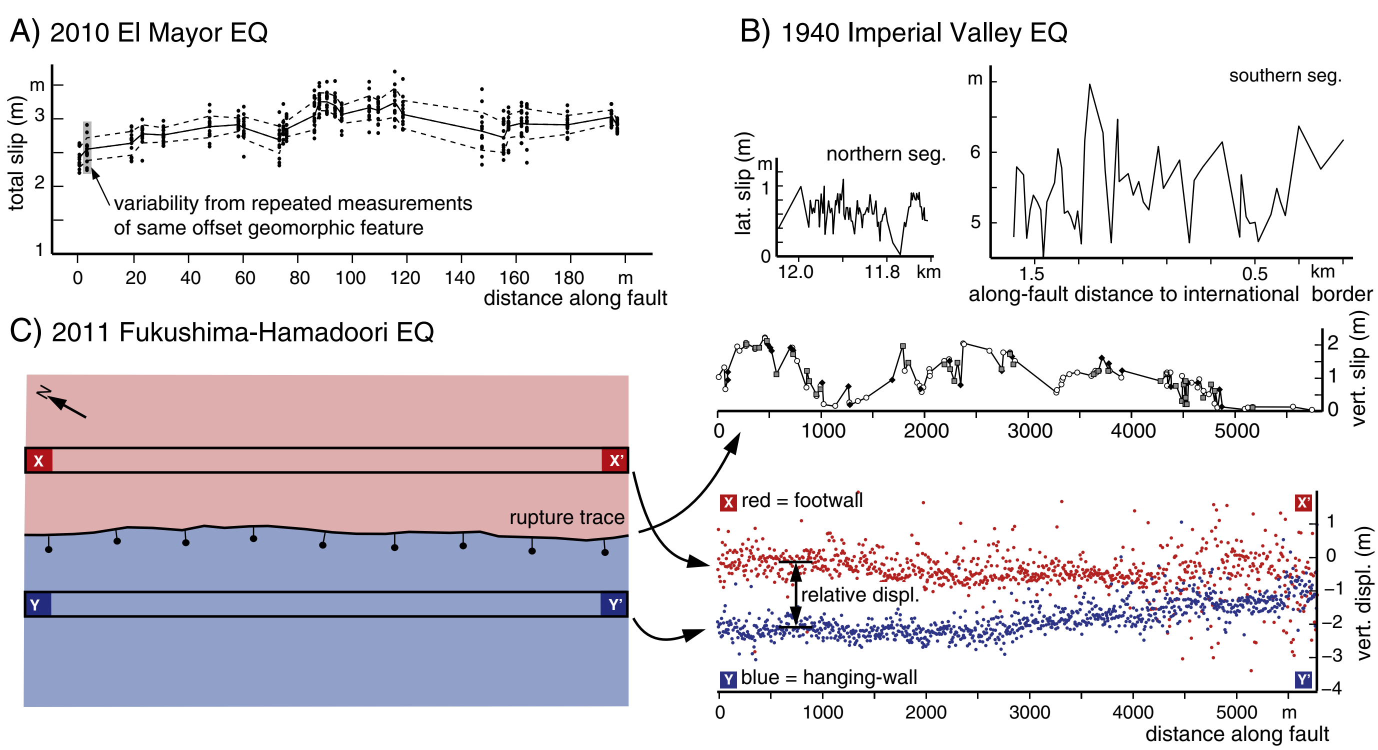

Fig. 9. Examples for along-fault single-event surface slip observations at different spatial scales. A) A section of the 2010 El Mayor earthquake, Mexico that was analyzed by Gold et al. (2013b). Repeated measurement revealed an aleatoric uncertainty of ~10–15% deviation (2σ) from a feature's mean offset value, exemplifying difficulties in identifying and projecting pre-EQ morphology. B) Two sections of the 1940 Imperial Valley rupture trace, California (Rockwell and Klinger, 2013), both exhibiting distinctly different slip amounts in this event. Slip varied by up to 30% from the respective section mean, presumably related to both aleatoric and epistemic uncertainty contributions. The short (e.g., <100 m) length-scales of this variation suggest very shallow along-fault locations of the causative slip anomalies. C) Section of the 2011 Hamadoori (Japan) EQ surface rupture trace and the corresponding near-fault displacement field derived through lidar-differencing (Mizoguchi et al., 2012; Nissen et al., 2014; Toda and Tsutsumi, 2013). While the along-fault surface displacement exhibits a high degree of offset variability at sub-km length-scales, the near-fault displacement is very smooth.

Please cite this article as: Zielke, O., et al., Fault slip and earthquake recurrence along strike-slip faults — Contributions of high-resolution geomorphic data, Tectonophysics (2014), http://dx.doi.org/10.1016/j.tecto.2014.11.004

of near-surface rheology to coseismically imposed high strains rather than reflecting rupture characteristics at seismogenic depths. This assumption is supported by data from the M6.6 Fukushima–Hamadoori EQ of 2011 in Japan. Surface rupture and along-fault slip distribution were documented for this normal faulting event (Mizoguchi et al., 2012; Nissen et al., 2014; Toda and Tsutsumi, 2013), revealing the aforementioned high variability in along-fault surface slip at sub-km length-scales (Fig. 9c). Lidar differencing by Nissen et al. (2014) further revealed that the displacement field determined across a few hundred meter aperture was much smoother — exhibiting a gradual taper of slip from NW to SE (Fig. 9C). This discrepancy in displacement variability (on- vs. off-fault) indicates that the corresponding physical sources must be located at very shallow depths along the rupture plane. This line of thought is supported by dislocation theory (e.g., Chinnery, 1961; Okada, 1992), indicating that the amplitude and spatial wavelength at which a slip anomaly is expressed at the surface are inversely proportional to the depth of the anomaly (Fig. 10). Thus, the spatial scales at which those high variations of along-fault surface slip are observed, rule out a direct relation to rupture controlling parameters at seismogenic depths.

Recent studies show that surface-slip may exhibit another level of along-fault variability. At few-km to 10s-of-km length-scales, observed surface slip may exhibit a roughly sinusoidal distribution (Fig. 11), where mean slip is more or less constant within a certain reach of the fault (i.e., not considering the aforementioned high-frequency along-fault offset variability) but then changes at the boundaries of those reaches (Elliott et al., 2012; Haeussler et al., 2004; Klinger et al., 2006; McGill and Rubin, 1999; Quigley et al., 2010; Rockwell et al., 2002; Zachariesen and Sieh, 1995). Those long-wavelength changes in along-fault surface slip have been attributed to more or less significant and spatially extensive changes in constitutive parameters that govern the rupture process at seismogenic depths and to fault geometric complexities such as fault terminations, step-overs, fault bends, or existence of multiple active fault traces, causing for example an increase in off-fault deformation and “damage” at the expense of along-fault slip at those locations (e.g., Klinger et al., 2006; Oskin et al., 2012). Fault reaches that are bounded by those changes in along-fault surface slip are considered fault segments (Fig. 11). It is reasonable to assume a positive correlation between the amount of observed along-fault variation in mean slip and the magnitude to which those rupture controlling parameters change: segment boundaries that reflect distinct changes in those parameters exhibit a more severe sinuosity (i.e., larger changes in mean along-fault surface slip) and vice versa. Considering how fault zone properties change as a fault matures (e.g., by accumulating an increasing amount of slip), fault segmentation evolves over geologic time scales as well (Candela et al., 2012; Klinger, 2010; Stirling et al., 1996; Wesnousky, 1988, 2006). Structurally mature faults will in general present a smaller number of segment boundaries, hence causing only subdued (and eventually absence of) sinuosity in along-fault surface slip distribution and vice versa.

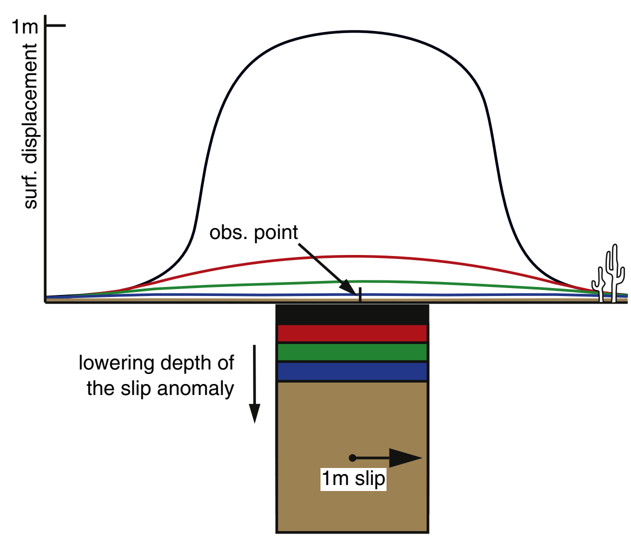

Fig. 10. Along-fault surface displacement due to a 1 m slip anomaly positioned at different depths (Okada, 1992). Color-coding of the lines relates to color-coding of the respective fault plane (i.e., slip anomaly). Surface displacement quickly decreases as the depth of the anomaly is increased. In order to re-generate the offset amplitude of the “black” displacement line, for example at the indicated observation point, with slip along the “red” slip anomaly patch (higher depth), a distinctly larger slip amount (e.g., by a factor of 10) is required. In this case, the resulting along-fault displacement would be distinctly more widespread (less discrete/sharp than the “black” case). These simple visualizations highlight that sources of offset variability must be located at very shallow depths in order to generate the observed variability at sub-km length-scales (Fig. 9).

Lastly, slip distributions at along-fault rupture terminations often resemble “dogtails” or “rainbows”, presumably related to terminus location relative to fault segment boundaries (e.g., Ward, 1997; Wesnousky, 2006). Ruptures terminating at a segment boundary may form concave-up (rainbow) slip distributions, while ruptures that were able to jump across a segment boundary but stop in the middle of a fault segment may form convex-up (dogtail) slip distributions (Fig. 11). The 1940 and 1979 Imperial Valley EQs, 1992 Landers EQ, as well as the 2002 Denali EQ, and 2010 Darfield EQ provide good examples for those styles of slip terminations and their relation to fault segmentation (e.g., Elliott et al., 2012; Haeussler et al., 2004; Schwartz et al., 2012; Sieh, 1996; Sieh et al., 1993). The scenario in which a rupture was able to jump across a segment boundary to form a “dogtail”-like slip distribution near the rupture termination has been described previously as “slip leakage” (Sieh, 1996). This term refers to the partial rupture of a fault segment, where only a portion of a segment's fault plane is slipping during an EQ (e.g. Figs. 1, 12). As a consequence, stratigraphic and geomorphic records may contain evidence of surface rupturing EQs that is not related to full rupture activation of the corresponding fault segment but for example more closely relates to full rupture activation along a neighboring fault segment. Such a superposition of recurrence signals from different sources may indicate complex EQ recurrence characteristics, especially in cases where partial rupture may be considered a persistent phenomenon—for example in areas with dense, interacting fault networks.

Single-event surface slip distributions vary at different spatial scales. Much of the observed variability occurs at sub-km length-scales and is related to a) difficulties in consistently projecting an assumed pre-EQ marker morphology onto an idealized fault plane, and b) slip anomalies whose source is located at (very) shallow depths. This length-scale of along-fault slip variability is not related to changes in rupture controlling at seismogenic depths — which is what we are most interested in as those dominate rupture initiation and strain renewal. Hence, much of the identified variability masks the mean slip-per-event for a given fault segment. While it may be relatively simple to extract the mean surface slip amount of a recent rupture along a given fault segment – for which many offset measurements can be taken – it becomes distinctly more difficult for older ruptures — for which only a few offset markers may have remained in the geomorphic record.

4.2. Multi-event slip accumulation

Few studies have utilized the potential of high-resolution lidar data so far to constrain along-fault slip accumulation. This is in part reasoned by the high ground resolution (<0.5 m) (Arrowsmith and Zielke, 2009; Lin et al., 2013) and along-fault spatial coverage, which are required for such an analysis. Even if data are available, it requires specific geomorphic conditions that enable to frequently form geomorphic markers and then preserve them for multiple EQ cycles. Those delicate conditions then need to coincide with a tectonically active fault that frequently displaced those geomorphic markers. Such conditions are not often met and so far slip-accumulation studies were situated preferentially in arid or semi-arid environments (largely related to the generally

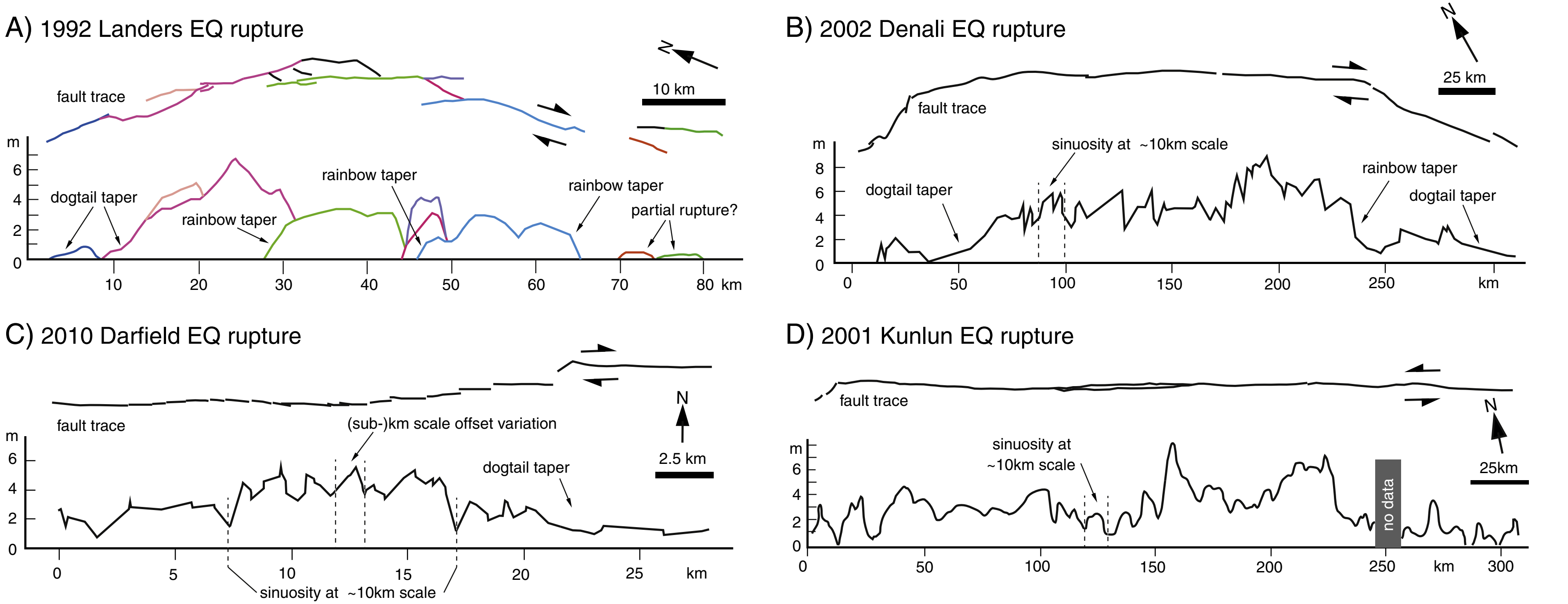

Fig. 11. Rupture trace and along-fault surface slip distributions of four dominantly strike-slip earthquakes. A) The 1992 Landers EQ activated multiple faults (Sieh et al., 1993) and its rupture is therefore segmented (color-coding relates fault trace and corresponding along-fault slip observation). Surface slip features "dogtail"- and "rainbow"-like distributions near rupture terminations along individual fault segments. An overall low slip amount along some ruptured sections (e.g., between km's 70 to 80) suggests an only partial activation of respective fault planes. B) Slip along the 2002 Denali EQ surface rupture also exhibits a high level of offset variability (Haeussler et al., 2004; Schwartz et al., 2012), also featuring "rainbow"-like distributions at segment boundaries and "dogtail"-like distributions when rupturing into a neighboring segment. At ~10 km and larger length-scales, slip varies in a roughly sinusoidal fashion. Aside from this sinusoidal distribution is slip along larger sections roughly constant. C) Surface slip distribution due to the 2010 Darfield EQ (Elliott et al., 2012; Quigley et al., 2010), with sub-km length-scale variation of slip that superposes an approximately constant slip value at ~10 km length-scales. Slip progressively decreases towards the East of the rupture trace, forming a weak expression of a "dogtail"-like slip taper which suggests that this portion of the fault ruptured only partially. This suggestion is supported by source inversion results (Elliott et al., 2012). D) Slip distribution fluctuation at ~10 km length-scales is well expressed for the 2001 Kunlun EQ (Klinger et al., 2006).

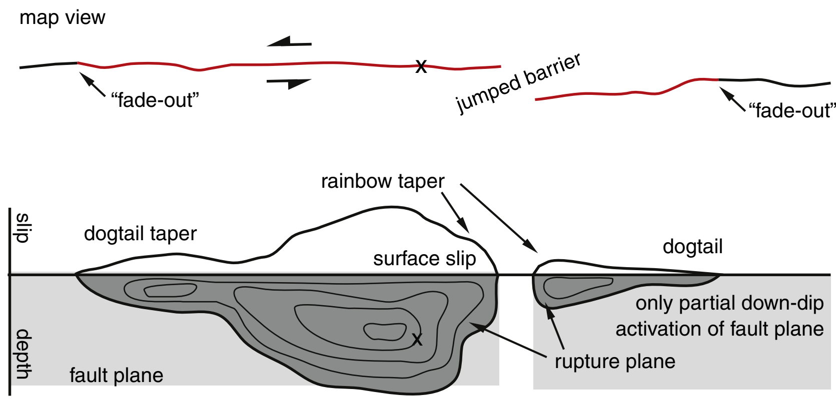

Fig. 12. Schematic representation of full rupture and partial fault activation (contour lines indicate fault slip), the latter for example due to slip leakage (i.e., jumping a fault segment boundary) and resulting surface slip distributions at rupture termination points. Rupture termination at a segment boundary frequently generates a "rainbow"-like surface slip termination (when "running into" the boundary), while termination within a fault segment (when slip is progressively fading out) is frequently expressed by a "dogtail"-like surface slip taper. These surface slip patterns relate to the depth extent of failure, where "dogtail"-like shapes indicate that the underlying fault plane was only partially activated along down-dip extension (Ward, 1997; Zielke and Arrowsmith, 2008).

higher preservation potential). However, recent studies for example in New Zealand (in moderate to humid conditions; Beauprćtre et al., 2012; DePascale et al., 2014; Langridge et al., 2014) indicate that other (non-arid) climatic regions may be exploited for this type analysis as well.

A recent study by Zielke et al. (2010) and elaborated in Zielke et al., (2012) along the Carrizo section of the south-central SAF used the B4 lidar data set (Bevis et al., 2005) to (re-)evaluate the surface slip distribution, associated with the most recent earthquake (the M7.8 Fort Tejon earthquake of 1857) and preceding ground-rupturing events. Based on a 0.5 m ground resolution DEM, Zielke et al. (2010) remotely identified and measured approximately 140 offset geomorphic markers with offsets <50 m along this ~60 km long section, more than 70 of which with displacements below 10 m. For each identified marker, an optimal offset value and an offset range were provided. Following the general conceptual approach by McGill and Sieh (1991), those values then define an offset probability density function (PDF), quantifying the range of plausible offsets. Zielke et al. (2010) revealed that the geomorphic slip along the Carrizo section during the great M7.8 earthquake of 1857 was with 5.3 +/− 1.4 m (2σ) distinctly lower than the previously reported 8–10 m that were derived based on air photo interpretation and field observation (e.g., Sieh, 1978; Wallace, 1968). Notably, the geomorphic expression of the 1857 event is subtle compared to the dominant 8–10 m offsets, as was also noted by Wallace (1968), possibly reflecting different levels of storm severity preceding the respective earthquakes (e.g., Grant Ludwig et al., 2010; Zielke et al., 2010). Slip along the Carrizo segment during the 1857 event also experienced the aforementioned offset variability at sub-km length-scales where offsets deviate from the mean by >1 m over 10s to 100 s of meters along the fault. Three-dimensional offset reconstructions based on excavations along the Carrizo section at Wallace Creek (Liu et al., 2004; Liu-Zeng et al., 2006) and at Phelan Creek (Grant and Sieh, 1993) have reported higher displacement values for the 1857 earthquake (7.8–8.0 m and 6.6–6.9 m respectively). One might argue that those trench sites happen to be in places that experienced high displacements due to the aforementioned along-fault offset variability at sub-km length-scales that is related to very shallow sources and non-elastic response (and spatial variation thereof) of surface material. For comparison, the nearest geomorphic offset measurements – taken less than 100 m away from those trench sites – were 5.0 +/− 0.7 m (2σ) for Wallace Creek and 5.7 +/− 1.0 m (2σ) for Phelan Creek. One might also argue that the stratigraphically-derived offsets include an additional slip component related to a pre-1857 EQ. While stratigraphic evidence does in fact suggest that those displacements were formed during the 1857 EQ (Grant and Sieh, 1993; Liu et al., 2004; Liu-Zeng et al., 2006), their age has not been constrained independently (i.e., via radiometric dating techniques), making this statement permissible. Further investigation is advocated to resolve the discrepancy of those different observations.

Aside from the MRE event, many additional displaced features were identified, constraining the slip accumulation pattern along this fault section. To analyze the slip accumulation pattern, Zielke et al. (2010) calculated the cumulative offset probability density (*COPD;* e.g., McGill and Sieh, 1991), summing the offset PDFs that were assigned to individual geomorphic markers. This approach revealed 5–6 clearly separated *COPD* peaks, centered at 5.3, 9.8, 14.9, 20.1, 24.6, and ~31 m of (right-lateral) displacement (Fig. 13A). Those peaks are well separated, indicating that few to none of the offset features have displacements falling in between *COPD* peaks. We adopted a Monte-Carlo approach to formally determine the mean slip-per-event while properly propagating the associated uncertainties, taking the identified *COPD* center value and corresponding peak half-width (considered to represent 1σ) to sample from a Gaussian distribution (e.g., Madden et al., 2013). The SOM to this paper contains the utilized MATLAB-script. Following this approach we find that we can explain the geomorphic offset along this section of the SAF with repeated offsets of 5.1 +/− 1.1 m (1σ). As is apparent from the *COPD* peaks, offsets – as resolved in the geomorphic record – repeat in ~5 m increments.

It is convenient to use the coefficient of variation, *CV* (e.g., Biasi, 2013; Goes and Ward, 1994; Hecker et al., 2013; Scharer, 2013) to express variation in a data set in a normalized, non-dimensional way. It is calculated as

$$CV = std(data)/mean(data) \tag{2}$$

where *std(data)* and *mean(data)* are data standard deviation and mean respectively. Defining the *CV* serves two purposes. First, it measures regularity in a data set. Following Goes and Ward (1994) and Scharer (2013) we provide a graphical representation of *CV* (Fig. 14), where the distance between individual horizontal lines may be considered the slip-per-event at a point along a fault (or the inter-event time when EQ timing is considered). A value of $CV = 0$ represents perfect regularity whereas $CV = 1$ indicates random (Poissonian) behavior. $CV > 1$ represents clustering. The *CV* is a non-dimensional quantity, enabling us to compare levels of regularity from different data sets such as the regularity in slip-per-event and the regularity in earthquake inter-event time. Hence, the *CV* provides a convenient tool to compare data set regularity. However, it is important to keep in mind how the values that were used to calculate the *CV* are derived. For example, the offset ranges that are assigned to individual offset measurements directly affect the *COPD* half-width and thus the standard deviation of mean slip recurrence. They contain uncertainties related to natural offset

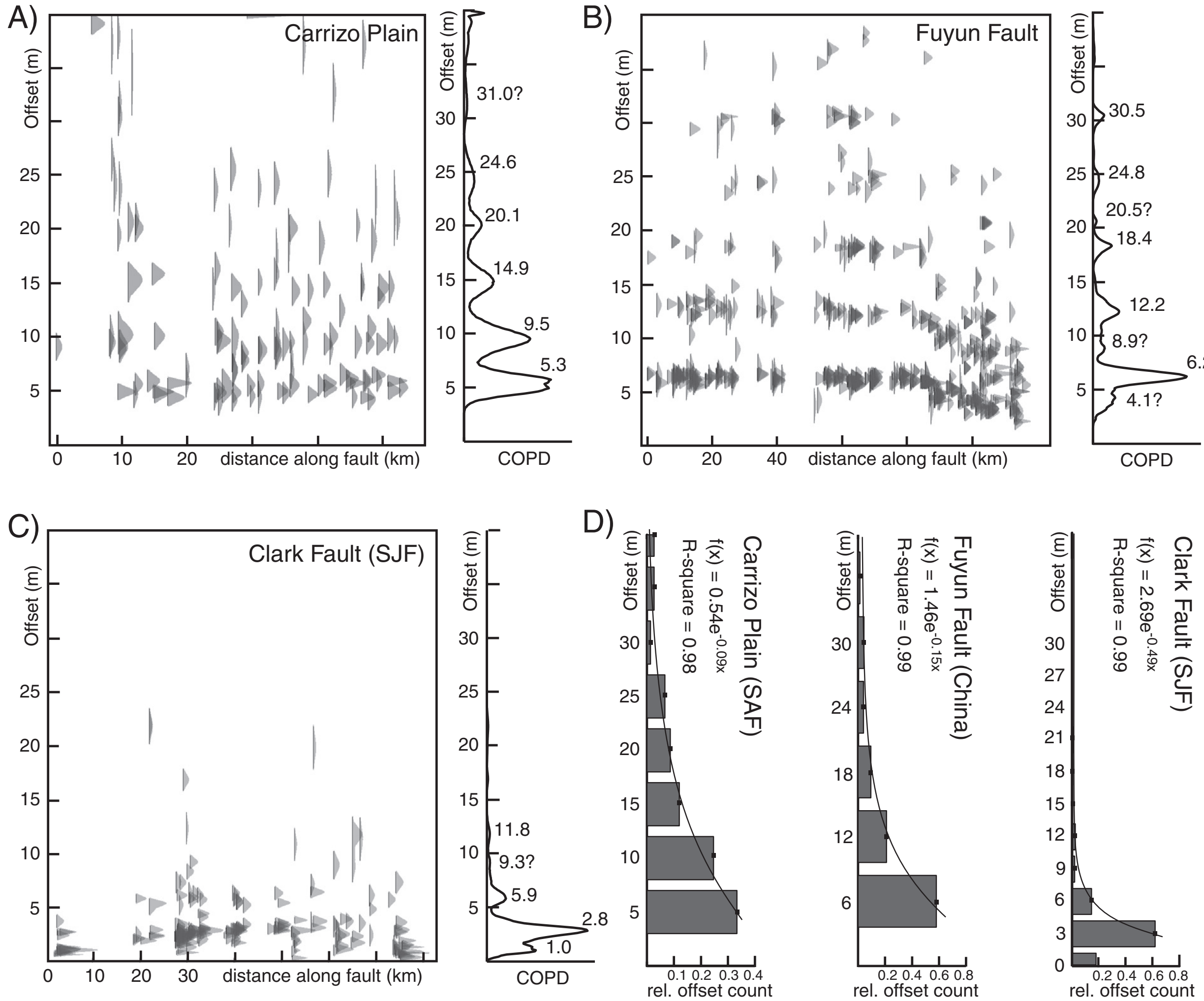

Fig. 13. Along-fault plot of offset PDFs from selected sites, discussed in the main text. PDF area is scaled with quality rating. Individual offset PDFs are summed to generate a *COPD* (cumulative offset probability density) plot. Clear and well-separated *COPD* peaks are indicative of surface slip-accumulation pattern. Carrizo Plain (A; Zielke et al., 2010) and Fuyun Fault (B; Klinger et al., 2011) show a quasi-periodic repetition of geomorphically recorded offset. For the Clark Fault (C; Salisbury et al., 2012), the few offset observations with higher slip amounts do not produce clear *COPD* peaks. Nonetheless, based on the provided data Salisbury et al. (2012) suggest 3 m offset increments. D) Histogram of offset observations per observed peak and exponential regression. While the exponential parameters vary for those different study regions, the exponential decay itself is solid (as is indicated by R-square fitting parameter). The first of those parameters expresses the production rate (e.g., 0.54), the second the decay rate (e.g., −0.09).

variability and the inherent difficulty of interpreting measuring offsets hundreds to thousands of years after their formation. Further, the offset range that reasonably well reconstructs a displaced feature is generally assigned "manually" and thus potentially subject to bias. Those aspects need to be considered when using *CV* as a metric for slip-per-event regularity.

As for the observed offsets along the Carrizo Plain we calculate the *CV* for slip $CV_s = 0.22$ — indicating a quasi-regular recurrence of large (~5 m) surface slip increments. Paleoseismic investigations at the Bidart Fan site along the Carrizo Plain fault segment (e.g., Akçiz et al., 2010) identified a ~90 +/−45 year mean recurrence interval of surface-rupturing earthquakes. Based on the corresponding EQ age PDFs, Biasi (2013) calculated a CV_t of 0.6 for the recurrence time of surface rupturing EQs at this site (Scharer, 2013). Note the distinct difference between CV_s and CV_t. While the amount of (surface) slip-per-event along the Carrizo Plain appears to be quasi-regular, the recurrence rate of surface-rupturing EQs is quite irregular. Further, the short mean recurrence rate of ~90 years implies that not every surface-rupturing EQ generated a ~5 m offset (Akçiz et al., 2010). Otherwise, a slip-rate of >50 mm/yr would be required which is almost twice the Holocene and geodetically derived well-constrained rate of motion (both being ~30–34 mm/yr; Freed et al., 2007; Noriega et al., 2006; Savage and Lisowski, 1995; Schmalzle et al., 2006; Sieh and Jahns, 1984). This implication extends to other paleoseismic sites along the southern SAF for example at Frazier Mountain (Scharer et al., 2014b), at Pallett Creek (e.g., Biasi et al., 2002; Scharer et al., 2011; Sieh et al., 1989), and at Wrightwood (e.g., Weldon et al., 2004, 2005; Scharer et al., 2010), exhibiting similarly high mean recurrence rates of surface rupture (ranging from ~70 to ~120 years) and similarly high CV_t values between 0.6 and 0.7 (Biasi, 2013; Scharer, 2013).

Considering the southern SAF recurrence rates for surface-rupturing EQs relative to the amount of slip that the respective sites have experienced in the MRE (the 1857 EQ), it becomes evident that not every surface rupturing EQ (along the south-central SAF) generates large, 1857-like slip at those sites. There is no one-to-one correlation between *COPD* peaks and EQ ages identified in paleoseismic excavations. Some of the EQs identified in those excavations must be associated with lower amounts of slip, not resolvable in the geomorphic record and hence not resolved in *COPD* plots. One possible explanation is partial fault rupture due to slip leakage as discussed earlier (Fig. 12). Those partial rupture EQs might cause surface rupture along respective fault segments (thus leaving their record in the disrupted stratigraphy), but the overall slip amount may be too small and its along-fault distribution too limited to enable their resolution from the geomorphic record (see discussion in Akçiz et al., 2010; Scharer et al., 2014b; Zielke et al., 2010).

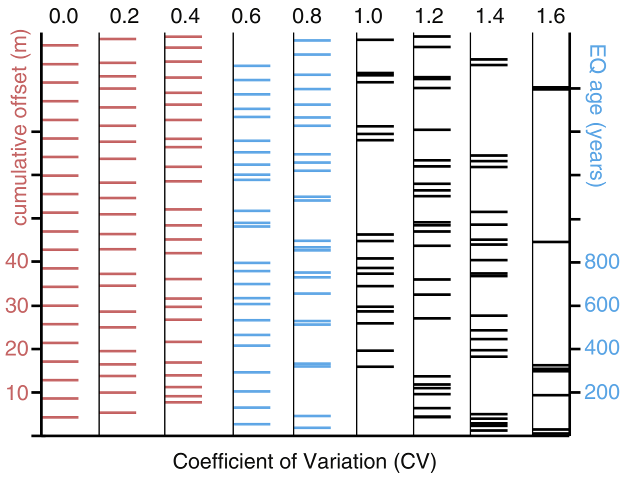

Fig. 14. Graphical representation of different levels of coefficient of variation *CV*, where a value of 0.0 expresses a perfectly regular repetition (for example of slip increment or inter-event time). A value of 1.0 represents a purely random behavior. The presented geomorphically derived data of along-fault offset accumulation frequently exhibit CV_s values <0.3 (respective range is indicated by in red) while the stratigraphically derived data of surface-rupture inter-event time frequently exhibit CV_t values >0.6 (range indicated in blue, see text). Along-fault surface slip accumulation appears to be distinctly more regular than the occurrence time of surface-rupturing EQs.

Klinger et al. (2011) investigated the Fuyun Fault in China, which ruptured in a large Mw8.0 earthquake in 1931. The mapped surface rupture of this event was more than 160 km long. Based on high-resolution satellite imagery (Quickbird imagery with 0.6 m ground resolution), Klinger et al. (2011) identified 290 laterally displaced features that were associated with the MRE, constraining the slip of the MRE to be 6.3 +/− 1.2 m (2σ). In total, more than 570 offset measurements were taken along the Fuyun Fault, resulting in surface-slip reconstructions for the MRE and 4 preceding events (Fig. 13B). Performing the same analysis as for the Carrizo Plain (using *COPD* peaks and respective peak half-width and then sampling in a Monte-Carlo approach from those PDFs) we determined 6.2 +/− 0.8 m (1σ) of slip-per-event. The resulting CV_s of 0.13 indicates a remarkably regular repetition of surface slip. Klinger et al. (2011) further noted that the number of displaced features (identified within a certain offset range) was inversely proportional to the offset amount. This observation was attributed to the potential of the surface morphology to preserve those tectonic signals and an exponential decay function was introduced to quantify the preservation potential.

Salisbury et al. (2012) measured offset geomorphic markers along the ~80 km long Clark fault, one of the major strands of the San Jacinto Fault (SJF), CA in the field and remotely from lidar data to estimate slip-per-event. Almost 170 displaced markers were identified. Salisbury et al. (2012) found that the most recent earthquake along the Clark fault generated 2.5–3 m of right-lateral slip. They further identified clusters of cumulative slip amounts at ~6 m and possibly at ~9 m and ~12 m (Fig. 13C), suggesting that slip along the Clark fault recurs in multiples of ~3 m. Using those *COPD* peaks, we computed mean slip of 3.0 +/− 0.7 m (1σ), in accordance with results by Salisbury et al. (2012). The corresponding CV_s value is 0.23, similar to that for the Carrizo Plain. Based on those surface slip observations, Salisbury et al. (2012) suggest that the Clark Fault typically fails during large EQs completely, thus exhibiting regularity in slip-per-event. Additional to this essentially characteristic behavior of full -rupture earthquakes (Fig. 1), they suggest that portions of the fault may also fail in smaller (partial rupture) earthquakes as was exemplified historically by the M_L 6.8 San Jacinto earthquake of 1918 which broke a ~20 km long section of the Clark fault with mean slip of 1.2 m (e.g., Salisbury et al., 2012). A corresponding sub-peak in *COPD* at ~1 m can be attributed to this event (Fig. 13C). Extensive paleoseismic excavations along the SJF at the Hog Lake site exposed evidence of 21 surface rupturing EQs that occurred within the last ~4000 years (Rockwell et al., 2014). The average recurrence interval for all ruptures during this period is ~185 +/− 105 years (2σ) resulting in a CV_t value of 0.63 (Rockwell et al., 2014). Similar to the aforementioned Bidart Fan site, we find a large discrepancy between CV_t and CV_s values for this fault.

As part of the UCERF3 project (Field et al., 2013), 53 sub-sections of the SAF system with airborne lidar coverage were mapped and surveyed to constrain respective MRE slip as well as slip-per-event from displaced geomorphic markers (Madden et al., 2013). Based on those data, we computed CV_s values for 17 of those sections – sections with at least 3 documented offset clusters – revealing a distinct range (~0.1 to ~0.6) of CV_s values that are centered at ~0.33. These CV_s values indicate a more variable slip recurrence when compared to the highlighted sites along the SAF (Carrizo Plain), Fuyun Fault, or SJF (Fig. 13) but still indicate slip accumulation in essentially regular slip increments. The UCERF3 project also included calculation of CV_t values for 32 paleoseismic sites along the SAF system (Biasi, 2013). The reported CV_t values are commonly between 0.6 and 0.8 (Scharer, 2013), which is again distinctly higher than the reported values for CV_s. Even though the presented data set can be considered relatively limited, there seems to be a commonality here, which is that the increments at which of surface slip recurs (constrained by CV_s value) are distinctly more regular than the inter-event time for surface rupturing EQs (constrained by CV_t value).

The number of offset observations and their relation to corresponding offset value is an important outcome of these studies. As discussed initially by Wallace (1968) and more formally by Klinger et al. (2011) and Zielke et al. (2012), the number of displaced features decays exponentially with increasing accumulated fault slip amount (thus with increasing time). Fig. 13 provides normalized offset observation histograms and exponential regressions to those data. While formation rate and preservation rate (Fig. 9) vary for different areas (defined by the coefficient and the exponential factor respectively), the exponential nature of the decay function itself is well established (as is indicated by the R-square metric of regression quality, Fig. 13). While production rate along the Clark Fault is highest (in relation to Carrizo and Fuyun), it also shows the highest decay function (and thus lowest preservation potential). For Carrizo and Fuyun, respective rates are comparable (within a factor of 2–3).

The exponential decay of *COPD* peaks highlights an inherent limitation when attempting to extend the surface-rupture record into the past from geomorphic data. Extending the record requires not only good preservation potential (low decay coefficients) but also a high marker production rate. The ideal landscape would thus be morphologically "fast" (dynamic) to provide a high marker production rate, while at the same time being morphologically "slow" to provide a high preservation potential. Because the decay can be described by a single gradual/asymptotic function (the exponential), the marker production rate is considered to remain constant (over the time period covered by the geomorphic record) or changes gradually over time. If the prior is assumed (approx. constant marker formation rate over inter-event time scales) then it would be possible to very crudely approximate the time of next (large) earthquake by comparing number of fresh markers (that exhibit no displacement and are thus considered younger than the MRE) with the exponential decay function —at least if the time of the MRE is known.

5. Discussion

As became clear within the last decade and exemplified by the studies highlighted in this paper, high-resolution topographic and optical data sets, in combination with paleoseismic investigations, provide the means to further improve our understanding of EQ recurrence and slip distribution characteristics. Slip varies at numerous spatial scales. Some of this variability – the sub-km length-scale variation around a fault section's mean – is related to local site effects, for example due to variations in site response related to the coseismically induced strains and due to near-surface variations in fault geometric parameters. The proximity of the respective slip anomalies close to the surface is indicated by the length-scales and amplitude changes (along-fault slip gradients) of the offset variability. Offset variability at sub-km length-scales therefore does not reflect rupture behavior at seismogenic depth. Along-fault offset observations at longer spatial wavelengths (few-km to 10s-of-km length-scales) on the other hand more closely relate to rupture controlling parameters at seismogenic depth. At those length-scales, fault segmentation is indicated by essentially constant surface slip along individual segments when activated in a full rupture earthquake (events that activate the full down-dip extend of the seismogenic zone or in other words the entire fault segment, e.g. Fig. 1). The aforementioned offset variability at sub-km length-scales superposes this quasi-constant offset amount at fault-segment length-scales and depending of relative amplitudes may effectively hide this underlying regular signal. Individual segments are separated by more or less strong slip gradients at segment boundaries. Those slip gradients correlate with changes in the rupture controlling parameters (at seismogenic depth). Single-event slip distributions serve as a template for interpretation of along-fault slip accumulation patterns.

The accumulation of geomorphic slip along the strike-slip fault (segments) that we examined is apparently regular. This is exemplified by the CV_s values we reported here, many of which < 0.3. The occurrence time of surface rupturing EQs on the other hand, is distinctly more variable. CV_t values are commonly > 0.6. How can this apparent discrepancy in behavior be explained? First, CV_s and CV_t were derived from different data sets, namely from the geomorphic and stratigraphic record. The minimum magnitude to generate surface rupture – and by that produce faulting evidence in stratigraphic and geomorphic records with cm-scale displacements in surface and sub-surface – has been estimated to be ~M5.5 (Bonilla, 1988; Wells and Coppersmith, 1994). At the surface, degradational processes will soon after the EQ obliterate those cm-scale disruptions of the ground, removing faulting evidence from the geomorphic record. At the sub-surface however, those disruptions may be well protected from erosional obliteration and remain in the corresponding stratigraphic record for extended periods of time. The same concept applies to larger earthquakes with higher along-fault slip amounts—degradational processes at the surface will generally more quickly obliterate faulting evidence than it occurs in the sub-surface. Based on this understanding and the presented data, we suggest that the common discrepancy between CV_s and CV_t values reflects the different resolution and preservation potential of stratigraphic and geomorphic record: not every earthquake that is identified in stratigraphic records finds its (resolved and preserved) expression in the geomorphic record. Aside from the potential obliteration of faulting evidence at the surface, other factors further contribute to this discrepancy in resolution potential. For example, the surface slip amount of some EQs may be too small to be resolvable in the geomorphology, especially when considering the high degree of along-fault offset variability at sub-km length-scales that we discussed and the resolution of the available topographic and optical imagery data on which they are measured. Also, in order to constrain the slip amount of an earthquake, a sufficient number of new geomorphic features must form prior to rupture (but after occurrence of the penultimate EQ). Hence, the stratigraphic record is more sensitive and more complete than the corresponding geomorphic record. In that regard, we may say that the stratigraphic record "sees" some aspect of fault behavior (i.e., rupture occurrence) for which the geomorphic record is or becomes "blind" over time. As a consequence of the different resolution potential, a one-to-one correlation between peaks in *COPD* and number of EQs that were identified in a paleoseismic excavation can generally not be assumed. In general, the first peak in *COPD* may not have formed due to occurrence of only one EQ; the second peak may not have formed due to occurrence of only two EQs and so forth.

While the difference in resolution potential may explain the differences between CV_s and CV_t, it does not explain why CV_s itself is relatively low — with values commonly < 0.3. A recent study by Hecker et al. (2013) also investigated the variability of slip-at-point along a fault by statistically analyzing a composite global data set of paleoseismic observations (i.e., primarily stratigraphic evidence of faulting as opposed to the geomorphic data that we used here). They reported a CV_s value of ~0.5 to be consistent with the data that were analyzed. This value is similar to the CV_t value (from stratigraphic record) that we reported (usually > 0.6) but distinctly higher than the CV_s value (from geomorphic record) that we found (usually < 0.3). We interpret this as further evidence of the different resolution potential of stratigraphic and geomorphic records. The CV_s value that is derived from stratigraphic data (Hecker et al., 2013) exhibits a higher variability than is expressed in the geomorphic record and by that apparently resolves an aspect of along-fault slip accumulation that is not "seen" in the geomorphology. The low CV_s value that we identified from geomorphic records indicates the existence of a slip increment whose apparent repetition may dominate the slip accumulation pattern along a given fault segment. If surface-slip accumulation is in fact dominated by repetition of a certain slip increment, then the slip contribution from those EQs that are not resolved in the geomorphic record (but where potentially identified in the stratigraphic record) to the overall slip budget of the fault segment must be small.

Fig. 15 provides a synoptic model that incorporates the aforementioned observations. In this model, slip-per-event at a point along a fault segment may vary from event to event. However, slip variation is not random but exhibits a bimodal signature, where the slip accumulation pattern and strain release are dominated by the occurrence of "full rupture" earthquakes, which are associated with "characteristic" slip increments (red lines, Fig. 15). Those slip increments are directly related to the rupture controlling parameters such as the constitutive properties along the fault plane, the fault geometric complexity of the fault plane, and the seismogenic width. Partial activation of a fault segment, for example due to slip leakage from a neighboring segment or due to failure of a portion of the fault segment, can generate surface rupture as well (blue lines, Fig. 15). Those partial rupture events do not contribute significantly to the overall strain release and slip accumulation and are thus not resolvable in the geomorphic record. They may however be identified in the stratigraphic record. As a result, the stratigraphic record would then contain the recurrence characteristics that relate a fault

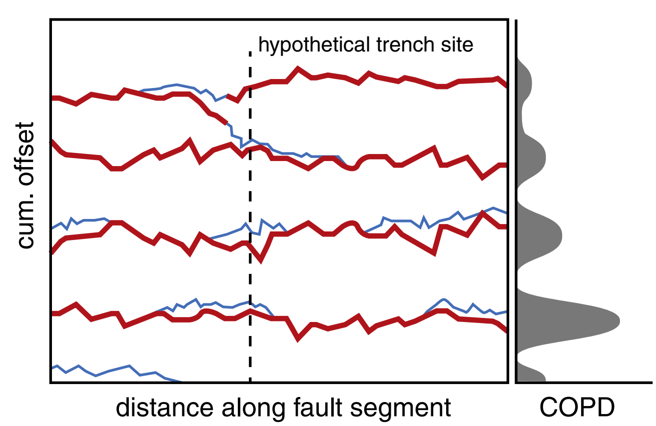

Fig. 15. Schematic representation of the slip accumulation along individual fault segments. While full rupture EQs (in red) occur quasi-regularly with respect to slip amount, the partial rupture EQs (in blue) occur more randomly along the fault with varying amount of slip and rupture length. Those smaller-scale surface ruptures may be related to slip leakage (Sieh, 1996) or occurrence of partial rupture (moderate-size) EQs, capable of breaking the ground surface (Pacheco et al., 1992; Zielke and Arrowsmith, 2008). Also shown are the corresponding peaks in *COPD*, indicating that the geomorphic record only resolves the FR events (red lines). Assuming a trench excavation along this hypothetical fault, evidence of the smaller events might be preserved in the stratigraphic record as well (see text for further discussion).

segments full rupture activation as well as its partial rupture activation where the latter may be a representation of full rupture occurrence along a neighboring segment that is leaking slip into the segment under consideration. Partial rupture EQs may be considered overtones or disturbances of an otherwise assumed more or less characteristic fault segment behavior. The presented model of slip accumulation along a fault segment (i.e., slip patch) is an extension of the characteristic earthquake and slip patch model (Schwartz and Coppersmith, 1984; Sieh, 1996), resolving some discrepancies between those models and newly acquired data on single-event surface slip distribution and along-fault slip accumulation patterns.

6. Conclusion

High-resolution topographic and optical imagery data have contributed to studies on along-fault slip distribution of recent EQs and slip accumulation patterns. The data sets will continue to improve, and their impact on our understanding of faulting will further increase. It is therefore important to reestablish the general requirements for offset determination from geomorphic record to ensure a common standard and comparability of different study results. We suggest measurement approaches and provide computational tools that increase the probability to generate meaningful offset reconstructions.

Our review of recent studies of single-event slip distributions and multi-event slip accumulation patterns, derived from geomorphic data, show that individual fault segments exhibit repetition of similar geomorphic offsets. These same-slip increments apparently dominate slip accumulation in order to explain the mismatch between CV_s and CV_t. The causative earthquakes activate the entire fault segment area. Fault segments rupture only partially, for example due to slip leakage from a neighboring segment or due to rupture along a portion of the fault segment. Those partial rupture earthquakes may be expressed in stratigraphic and possibly geomorphic records, but they contribute only marginally to the overall slip accumulation of the fault segment. We find it useful to limit models of slip accumulation pattern (i.e., earthquake recurrence) to individual fault segments, largely because of the inherent difficulties to constrain the end points of a surface-rupturing EQ from geomorphic evidence alone. Those difficulties are in part related to the high variability in slip along a rupture trace, for example at sub-km scales.

Supplementary data to this article can be found online at http://dx.doi.org/10.1016/j.tecto.2014.11.004.

Acknowledgments

We want to thank review paper coordinator Timothy Horscroft for inviting this manuscript for publication. We also want to thank David Schwartz and one anonymous reviewer, as well as the editor and associate editor for their efforts and suggestions which allowed us to further improve this manuscript. We further thank Kate Scharer and Glenn Biasi for inspirational discussions on *CV* calculation and interpretation. Discussions with David Haddad, George Hilley, Chris Madden Madugo, Barrett Salisbury, Tom Rockwell, and others have guided our thinking on these topics.

References

Akçiz, S.O., Grant Ludwig, L., Arrowsmith, J.R., Zielke, O., 2010. Century-long average time intervals between earthquake ruptures of the San Andreas Fault in the Carrizo Plain, California. Geology 38 (9), 787–790. http://dx.doi.org/10.1130/G30995.1.

Akyüz, H.S., Hartleb, R., Barka, A., Altunel, E., Sunal, G., Meyer, B., Armijo, R., 2002. Surface rupture and slip distribution of the 12 November 1999 Duzce Earthquake (M7.1), North Anatolian Fault, Bolu, Turkey. Bull. Seismol. Soc. Am. 92 (1), 61–66.

Allen, R.M., 2007. Earthquake hazard mitigation: new directions and opportunities. In: Schubert, Gerald (Ed.), Treatise on GeophysicsEarthquake Seismology vol. 4. Elsevier.

Allen, T.I., Wald, D.J., Earle, P.S., Marano, K.D., Hotovec, A.J., Lin, K., Hearne, M.G., 2009. An atlas of shakemaps and population exposure catalog for earthquake loss modeling. Bull. Earthq. Eng. 7, 701–718. http://dx.doi.org/10.1007/s10518-009-9120-y.

Arrowsmith, J.R., Zielke, O., 2009. Tectonic geomorphology of the San Andreas Fault Zone from high-resolution topography: an example from the Cholame segment. Geomorphology 113 (1), 70–81. http://dx.doi.org/10.1016/j.geomorph.2009.01.002.

Barth, N.C., Toy, V.G., Langridge, R.M., Norris, R.J., 2012. Scale dependence of oblique plate-boundary partitioning: new insights from Lidar, Central Alpine Fault, New Zealand. Lithosphere 4, 435–448. http://dx.doi.org/10.1130/L201.1.

Beauprćtre, S., Garambois, S., Manighetti, I., Malavieille, J., Sénéchal, G., Chatton, M., Davies, T., Larroque, C., Rousset, D., Cotte, N., Romano, C., 2012. Finding the buried record of past earthquakes with GPR-based paleoseismology: a case study on the Hope Fault, New Zealand. Geophys. J. Int. 189, 73–100. http://dx.doi.org/10.1111/j.1365-246X.2012.05366.x.

Beeler, N., Tullis, T.E., Weeks, J.D., 1994. The roles of time and displacement in the evolution effect in rock friction. Geophys. Res. Lett. 21 (18), 1,987–1,990.

Behr, W.M., Rood, D.H., Fletcher, K.E., Guzman, N., Finkel, R., Hanks, T.C., Hudnut, K.W., Kendrick, K.J., Platt, J.P., Sharp, W.D., Weldon, R.J., Yule, J.D., 2010. Uncertainties in slip-rate estimates for the mission creek strand of the Southern San Andreas Fault at Biskra Palms Oasis, Southern California. Geol. Soc. Am. Bull. 122 (9), 1360–1377. http://dx.doi.org/10.1130/B30020.1.

Ben-Zion, Y., 2008. Collective behavior of earthquakes and faults: continuum-discrete transitions, progressive evolutionary changes, and different dynamic regimes. Rev. Geophys. 46, RG4006. http://dx.doi.org/10.1029/2008RG000260.1.

Bevis, M., Hudnut, K., Sanchez, R., Toth, C., Grejner-Brzezinska, D., Kendrick, E., Caccamise, D., Raleigh, D., Zhou, H., Shan, S., Shindle, W., Yong, A., Harvey, J., Borsa, A., Ayoub, F., Shrestha, R., Carter, B., Sartori, M., Phillips, D., Coloma, F., 2005. *The B4 Project: Scanning the San Andreas and San Jacinto Fault Zones*, Abstract H34B-01 presented at 2005 Fall Meeting. AGU, San Francisco, Calif.

Biasi, G.P., 2013. Maximum likelihood recurrence intervals for California paleoseismic sites, in uniform California earthquake rupture forecast, version 3 (UCERF3) —the time-independent model. Appendix H, U.S. Geological Survey Open-File Report 2013–1165 (http://pubs.usgs.gov/of/2013/1165/).

Biasi, G.P., Weldon, R.J., Fumal, T.E., Seitz, G.G., 2002. Earthquakes on the Southern San Andreas Fault, California. Bull. Seismol. Soc. Am. 92 (7), 2,761–2,781.

Bilham, R., 2004. Urban earthquake fatalities: a safer world, or worse to come? Seismol. Res. Lett. 75, 706–712.

Blanpied, M.L., Lockner, D.A., Byerlee, J.D., 1991. Fault stability inferred from granite sliding experiments at hydrothermal conditions. Geophys. Res. Lett. 18 (4), 609–612.

Bonilla, M.G., 1988. Minimum earthquake magnitude associated with coseismic surface faulting. Bull. Assoc. Eng. Geol. 25, 17–29.

Brooks, B.A., Hudnut, K.W., Akçiz, S.O., Delano, J., Glennie, C.L., Prentice, C.S., DeLong, S., 2013. On offset stream measurements and recent coseismic surface rupture in the Carrizo section. Abstract T21D-01 presented at 2013 Fall Meeting. AGU, San Francisco, Calif.

Brown, M., Lowe, D.G., 2005. Unsupervised 3d object recognition and reconstruction in unordered datasets. Proceedings of the Fifth International Conference on 3-D Digital Imaging and Modeling, pp. 56–63.

Bruce, J.P., 1968. Atlas of rainfall intensity-duration frequency data for Canada. Climatol. Studies 8. Met. Branch, Dept. of Transport, Toronto.

Burbank, D.W., Anderson, R.S., 2012. Tectonic Geomorphology, 2nd edition. Blackwell Publishing Ltd., Oxford, U.K.

Candela, T., Renard, F., Klinger, Y., Mair, K., Schmittbuhl, J., Brodsky, E.E., 2012. Roughness of fault surfaces over nine decades of length scales. J. Geophys. Res. 117, B08409. http://dx.doi.org/10.1029/2011JB009041.

Carter, W.E., Shrestha, R.L., Slatton, K.C., 2007. Geodetic laser scanning. Phys. Today 41–47.

Chiba, T., Kaneta, S., Suzuki, Y., 2008. *Red relief image map: new visualization method for three dimensional data,* the international archives of the photogrammetry. Remote Sens. Spat. Inf. Sci. 37 (B2), 1071–1076.

Chinnery, M.A., 1961. The deformation of the ground around surface faults. Bull. Seismol. Soc. Am. 51 (3), 355–372.

Cowgill, E., 2007. Impact of riser reconstruction on estimation of secular variation in rates of strike-slip faulting: Revisiting the Cherchen River site along the Altyn Tagh fault. NW China. Earth Planet. Sci. Lett. 254, 239–255 http://dx.doi.org/10.1016.j.epsl.2006.09.015.

Crosby, C.J., Arrowsmith, J.R., Nandigam, V., Baru, C., 2011. *Online access and processing of LiDAR topography data* in Geoinformatics. In: Keller, G.R., Baru, C. (Eds.), Cyberinfrastructure for the Solid Earth Sciences. Cambridge University Press.

Dellaert, F., Seitz, S., Thorpe, C., Thrun, S., 2000. Structure from motion without correspondence. IEEE Computer Society Conference on Computer Vision and Pattern Recognition.

DePascale, G.P., Quigley, M.C., Davies, T.R.H., 2014. Lidar reveals uniform Alpine fault offsets and bimodal plate boundary rupture behavior, New Zealand. Geology 42 (5), 411–414 http://dx.doi.org/10.1130.

Dieterich, J.H., 1981. Constitutive properties of faults with simulated gauge. In: Carter, N.L., Friedman, M., Logan, J.M., Stearns, D.W. (Eds.), Mechanical Behavior of Crustal Rocks. Am. Geophys. Union, Geophys. Monogr. 24, pp. 103–120.

Elliott, J.R., Nissen, E.K., England, P.C., Jackson, J.A., Lamb, S., Li, Z., Oehlers, M., Parsons, B., 2012. Slip in the 2010–2011 Canterbury Earthquakes, New Zealand. J. Geophys. Res. 117, B03401. http://dx.doi.org/10.1029/2011JB008868.

Field, E.H., Biasi, G.P., Bird, P., Dawson, T.E., Felzer, K.R., Jackson, D.D., Johnson, K.M., Jordan, T.H., Madden, C., Michael, A.J., Milner, K.R., Page, M.T., Parsons, T., Powers, P.M., Shaw, B.E., Thatcher, W.R., Weldon, R.J., II, Y. Zeng, 2013. *Uniform California earthquake rupture forecast, version 3 (UCERF3) — The time-independent model*, U.S. Geological Survey Open-File Report 2013–1165 (http://pubs.usgs.gov/of/2013/1165/).

Fonstad, M.A., Dietrich, J.T., Courville, B.C., Jensen, J.L., Carbonneau, P.E., 2013. Topographic structure from motion: a new development in photogrammetric measurement. Earth Surf. Process. Landf. 38, 421–430. http://dx.doi.org/10.1002/esp.3366.

Freed, A.M., Ali, S.T., Bürgmann, R., 2007. Evolution of stress in Southern California for the Past 200 years from coseismic, postseismic, and interseismic stress changes. Geophys. J. Int. 169, 1,164–1,179. http://dx.doi.org/10.1111/j.1365-246X.2007.03391.x.

Glennie, C.L., Carter, W.E., Shrestha, R.L., Dietrich, W.E., 2013. Geodetic imaging with airborne lidar: the Earth's surface revealed. Rep. Prog. Phys. 76, 086801. http://dx.doi.org/10.1088/0034-4885/76/8/086801.

Goes, S.D.B., Ward, S.N., 1994. Synthetic seismicity for the San Andreas fault. Ann. Geophys. 37 (6), 1495–1513.

Gold, P.O., Cowgill, E., Kreylos, O., Gold, R.D., 2012. A terrestrial lidar-based workflow for determining three-dimensional slip vectors and associated uncertainties. Geosphere 8 (2), 431–442. http://dx.doi.org/10.1130/GES00714.1.

Gold, R.D., Stephenson, W.J., Odum, J.K., Briggs, R.W., Crone, A.J., Angster, S.J., 2013a. Concealed quaternary strike-slip fault resolved with airborne lidar and seismic reflection: the Grizzly Valley Fault System, Northern Walker Lane, California. J. Geophys. Res. 118, 3753–3766. http://dx.doi.org/10.1002/jgrb.50238.

Gold, P.O., Oskin, M.E., Elliott, A.J., Hinojosa-Corona, A., Taylor, M.H., Kreylos, O., Cowgill, E., 2013b. Coseismic slip variation assessed from terrestrial lidar scans of the El Mayor-Cucupah Surface Rupture. Earth Planet. Sci. Lett. 366, 151–162. http://dx.doi.org/10.1016/j.epsl.2013.01.040.

Grant, L., 2007. Historical seismicity — paleoseismology. In: Schubert, Gerald (Ed.), Treatise on GeophysicsEarthquake Seismology vol. 4. Elsevier.

Grant Ludwig, L., Akçiz, S.O., Noriega, G.N., Zielke, O., Arrowsmith, J.R., 2010. Climate modulated channel incision and rupture history of the San Andreas fault in the Carrizo Plain. Science 327, 1117–1119. http://dx.doi.org/10.1126/science.1182837.

Grant, L., Sieh, K.E., 1993. Stratigraphic evidence for seven meters of dextral slip on the San Andreas Fault during the 1857 Earthquake in the Carrizo Plain. Bull. Seismol. Soc. Am. 83 (3), 619–635.

Guidoboni, E., Comastri, A., Traina, G., 1994. *Catalogue of Ancient Earthquakes in the Mediterranean Area up to the 10th Century*. Phillips, B (trans.). Insituto Nazionale di Giofisica, Rome.

Gutenberg, B., Richter, C.F., 1954. Seismicity of the Earth and Associated Phenomena, 2nd ed. Princeton University Press, Princeton, N.J.

Haddad, D.E., Akçiz, S.O., Arrowsmith, J.R., Rhodes, D.D., Oldow, J.S., Zielke, O., Toke, N.A., Haddad, A.G., Mauer, J., Shilpakar, P., 2012. Applications of airborne and terrestrial laser scanning to paleoseismology. Geosphere 8 (4), 771–786. http://dx.doi.org/10.1130/GES00701.1.

Harding, D.J., Berghoff, G.S., 2000. Fault scarp detection beneath dense vegetation cover: airborne LiDAR mapping of the Seattle fault zone, Bainbridge Island, Washington. Proceedings of the American Society Photogrammetry and Remote Sensing Annual Conference, Washington, D.C. , p. 9.

Hartley, R., Zisserman, A., 2004. Multiple View Geometry in Computer Vision, 2nd ed. Cambridge University Press.

Haeussler, P.J., Schwartz, D.P., Dawson, T.E., Stenner, H.D., Lienkaemper, J.J., Sherrod, B., Cinti, F.R., Montone, P., Craw, P.A., Crone, A.J., Personius, S.F., 2004. Surface rupture and slip distribution of the Denali and Totschunda Faults in the 3 November 2002 M 7.9 Earthquake, Alaska. Bull. Seismol. Soc. Am. 94 (6B), S23–S52. http://dx.doi.org/10.1785/0120040626.

Haugerud, R.A., Harding, D.J., Johnson, S.Y., Harless, J.L., Weaver, C.S., 2003. High-resolution lidar topography of the Pudget Lowland, Washington. Geol. Soc. Am. Today 4–10 (June 2003).

Hecker, S., Abrahamson, N.A., Wooddell, K.E., 2013. Variability of displacment at a point: implications for earthquake-size distribution and rupture hazard on faults. Bull. Seismol. Soc. Am. 103 (2A), 651–674. http://dx.doi.org/10.1785/0120120159.

Hershfield, D.M., 1961. Rainfall frequency atlas of the United States, for durations from 30 minutes to 24 hours and return periods from 1 to 100 years. Tech. Paper No. 40. Weather Bureau, US Dept Commerce, Washington, DC.

Hilley, G.E., DeLong, S., Prentice, C., Blisniuk, K., Arrowsmith, J.R., 2010. Morphologic dating of fault scarps using airborne laser swath mapping (ALSM) data. Geophys. Res. Lett. 37, L04301. http://dx.doi.org/10.1029/2009GL042044.

Howle, J.F., Bawden, G.W., Schweickert, R.A., Finkel, R.C., Hunter, L.E., Rose, R.S., von Twistern, B., 2012. Airborne lidar analysis and geochronology of faulted glacial moraines in the Tahoe-Sierra Frontal Fault Zone reveal substantial seismic hazard in the Lake Tahoe Region, California-Nevada, USA. Geol. Soc. Am. Bull. 124 (7), 1087–1101. http://dx.doi.org/10.1130/B30598.1.

Hu, Y., 2003. Automated Extraction of Ditigal Terrain Models, Roads and Buildings Using Airborne Lidar Data. Department of Geomatics Engineering, Univerisity of Calgary, Canada (PhD dissertation).

Hudnut, K.W., Borsa, A., Glennie, C., Minster, J.-B., 2002. High-resolution topography along surface rupture of the 16 October 1999 Hector Mine, California Earthquake (Mw 7.1) from airborne laser swath mapping. Bull. Seismol. Soc. Am. 92 (4), 1570–1576. http://dx.doi.org/10.1785/0120000934.

Hutton, J., 1785. *The System of the Earth, its Duration and Stability*, Royal Society of Edinburgh. http://www.uwmc.uwc.edu/geography/hutton/Abstract-facsimile/abstract1.htm.

James, M.R., Robson, S., 2012. Straightforward reconstruction of 3D surfaces and topography with a camera: accuracy and geoscience application. J. Geophys. Res. 117, F03017. http://dx.doi.org/10.1029/2011JF002289.

Johnson, K., Nissen, E., Saripalli, S., Arrowsmith, J.R., McGarey, P., Scharer, K., Williams, P., Blisniuk, K., 2014. Rapid mapping of ultra-fine fault zone topography with structure from motion. Geosphere 10 (5), 1–18. http://dx.doi.org/10.1130/GES01017.1.

Keller, P., Kreylos, O., Vanco, M., Hering-Bertram, M., Cowgill, E.S., Kellogg, L.H., Hamann, B., Hagen, H., 2010. Extracting and visualizing structural features in environmental point cloud Lidar data sets, to appear. In: Pascucci, V., Tricoche, X., Hagen, H., Tierny, J. (Eds.), Topological Methods in Data Analysis and Visualization: Theory, Algorithms, and Applications (TopoInVis 2009). Springer-Verlag, Heidelberg, Germany.

King, G.C.P., Wesnousky, S.G., 2007. Scaling of fault parameters for continental strike-slip earthquakes. Bull. Seismol. Soc. Am. 97 (6), 1,833–1,840. http://dx.doi.org/10.1785/0120070048.

Klinger, Y., 2010. Relation between continental strike-slip earthquake segmentation and thickness of the crust. J. Geophys. Res. 115, B07306. http://dx.doi.org/10.1029/2009JB006550.

Klinger, Y., Xu, X., Tapponnier, P., Van der Woerd, J., Laserre, C., King, G.C.P., 2005. High-resolution satellite imagery mapping of the surface rupture and slip distribution of the Mw ~7.8, November 14, 2001 Kokoxili Earthquake (Kunlun fault, Northern Tibet, China). Bull. Seismol. Soc. Am. 95 (5), 1,970–1,987.

Klinger, Y., Michel, R., King, G.C.P., 2006. Evidence for an earthquake barrier model from MW ~7.8 Kokoxili (Tibet) earthquake slip-distribution. Earth Planet. Sci. Lett. 242, 354–364.

Klinger, Y., Etchebes, M., Tapponier, P., Narteau, C., 2011. Characteristic slip for five great earthquakes along the Fuyun Fault in China. Nat. Geosci. 4, 389–392. http://dx.doi.org/10.1038/NGEO1158.

Krishnan, S., Crosby, C., Nandigam, V., Phan, M., Cowart, C., Baru, C., Arrowsmith, JR., 2011. OpenTopography: a services oriented architecture for community access to LIDAR topography. International Conference on Computing for Geospatial Research and Application (http://portal.acm.org/citation.cfm?id = 1999327).

Langridge, R.M., Ries, W.F., Farrier, T., Barth, N.C., Khajavi, N., De Pascale, G.P., 2014. Developing sub 5-m Lidar DEMs for forested sections of the Alpine and Hope Faults, South Island, New Zealand: implications for structural interpretations. J. Struct. Geol. 64 (SI), 53–66.

LePrince, S., Barbot, S., Ayoub, F., Avouac, J., 2007. Automatic and precise orthorectification, coregistration, and subpixel correlation of satellite images, application to ground deformation measurements. IEEE Trans. Geosci. Remote Sens. 45 (6), 1529–1558.

LePrince, S., Hudnut, K.W., Akciz, S.O., Hinojosa-Corona, A., Fletcher, J.M., 2012. Surface rupture and slip variation induced by the 2010 El Mayor-Cucapah Earthquake, Baja California, quantified using COSI-Corr analysis on pre- and post-earthquake LiDAR acquisitions. AGU Fall Meeting Abstracts, EP41A–0596.

Lienkaemper, J.J., 2001. 1857 slip on the San Andreas Fault Southeast of Cholame, California. Bull. Seismol. Soc. Am. 91 (6), 1659–1672.

Lin, Z., Kaneda, H., Mukoyama, S., Asada, N., Chiba, T., 2013. Detection of subtle tectonic–geomorphic features in densely forested mountains by very high-resolution airborne lidar survey. Geomorphology 182, 104–115. http://dx.doi.org/10.1016/j.geomorph.2012.11.001.

Liu, J., Kinger, Y., Sieh, K.E., Rubin, C., 2004. Six similar sequential ruptures of the San Andreas Fault, Carrizo Plain, California. Geology 32 (8), 649–652. http://dx.doi.org/10.1130/G20478.1.

Liu-Zeng, J., Klinger, Y., Sieh, K., Rubin, C., Seitz, G., 2006. Serial ruptures of the San Andreas Fault, Carrizo Plain, California, revealed by three-dimensional excavations. J. Geophys. Res. 111, B02306. http://dx.doi.org/10.1029/2004JB003601.

Lowe, D.G., 2004. Distinctive image features from scale-invariant keypoints. Int. J. Comput. Vision 60 (2), 91–110.

Madden, C., Haddad, D.E., Salisbury, J.B., Zielke, O., Arrowsmith, JR., Weldon, R.J., Colunga, J., 2013. *Compilation of slip-in-the-last-event data and analysis of last event, repeated slip, and average displacement for recent and prehistoric ruptures*, in Uniform California earthquake rupture forecast, version 3 (UCERF3) — the time-independent model. Appendix R, U.S. Geological Survey Open-File Report 2013–1165 (http://pubs.usgs.gov/of/2013/1165/).

Madsen, H., Arnbjerg-Nielsen, K., Mikkelsen, P.S., 2009. Update of regional intensity-duration-frequency curves in Denmark: Tendency towards increase storm intensities. Atmos. Res. 92, 343–349. http://dx.doi.org/10.1016/j.atmosres.2009.01.013.

McCalpin, J., 2009. Paleoseismology, 2nd edition. Academic Press, San Diego, CA.

McGill, S., Rubin, C., 1999. Surficial slip distribution on the central emerson fault during the June 28, 1992 Landers Earthquake, California. J. Geophys. Res. 104 (B3), 4,811–4,833.

McGill, S., Sieh, K.E., 1991. Surficial offsets on the Central and Eastern Garlock fault associated with prehistoric earthquakes. J. Geophys. Res. 96 (B13), 21,597–21,621.

Menke, W., 2012. Geophysical Data Analysis: Discrete Inverse Theory, MATLAB edition, 3rd edition. Academic Press, San Diego, CA.

Miller, J.F., 1963. Probable maximum precipitation and rainfall-frequency data for Alaska. Tech. Paper No. 47. Weather Bureau, US Dept. Commerce, Washington, DC.

Mizoguchi, K., Uehara, S., Ueta, K., 2012. Surface fault ruptures and slip distributions of the Mw 6.6 11 April Hamadori, Fukushima Prefecture, Northeast Japan, Earthquake. Bull. Seismol. Soc. Am. 102, 1,949–1,956.

Nissen, E., Krishnan, A.K., Arrowsmith, J.R., Saripalli, S., 2012. Three-dimensional surface displacements and rotations from differencing pre- and post-earthquake lidar point clouds. Geophys. Res. Lett. 39, L16301. http://dx.doi.org/10.1029/2012GL052460.

Nissen, E., Maruyama, T., Arrowsmith, J.R., Elliott, J.R., Krishnan, A.K., Oskin, M.E., Saripalli, S., 2014. Coseismic fault zone deformation revealed with differential lidar: examples from Japanese Mw ~7 intraplate earthquakes. Earth Planet. Sci. Lett. 405, 244–256. http://dx.doi.org/10.1016/j.epsl.2014.08.031.

Noriega, G.R., Arrowsmith, J.R., Grant, L., Young, J.J., 2006. Stream channel offset and late holocene slip rate of the San Andreas Fault at the Van Matre Ranch Site, Carrizo Plain, California. Bull. Seismol. Soc. Am. 96 (1), 33–47. http://dx.doi.org/10.1785/0120050094.

Nur, A., 2007. Historical seismicity — archeoseismology. In: Schubert, Gerald (Ed.), Treatise on GeophysicsEarthquake Seismology vol. 4. Elsevier.

Okada, Y., 1992. Internal deformation due to shear and tensile faults in a half-space. Bull. Seismol. Soc. Am. 82 (2), 1,018–1,040.

Oskin, M.E., Le, K., Strane, M.D., 2007. Quantifying fault-zone activity in arid environments with high-resolution topography. Geophys. Res. Lett. 34, L23S05. http://dx.doi.org/10.1029/2007GL031295.

Please cite this article as: Zielke, O., et al., Fault slip and earthquake recurrence along strike-slip faults — Contributions of high-resolution geomorphic data, Tectonophysics (2014), http://dx.doi.org/10.1016/j.tecto.2014.11.004

Oskin, M.E., Arrowsmith, JR., Hinojosa-Corona, A., Elliott, A.J., Fletcher, J.M., Fielding, E.J., Gold, P.O., Javier Gonzalez Garcia, J., Hudnut, K.W., Liu-Zeng, J., Teran, O.J., 2012. Near-field deformation from the El Mayor-Cucupah earthquake revealed by differential lidar. Science 335, 702–705. http://dx.doi.org/10.1126/science.1213778.

Pacheco, J.F., Scholz, C.H., Sykes, L.R., 1992. Change in frequency-size relationship from small to large earthquakes. Nature 355, 71–73.

Quigley, M., Van Dissen, R., Villamor, P., Litchfield, N., Barrell, D., Furlong, K., Stahl, T., Duffy, B., Bilderback, E., Noble, D., Townsend, D., Begg, J., Jongens, R., Ries, W., Claridge, J., Klahn, A., Mackenzie, H., Smith, A., Hornblow, S., Nicol, R., Cox, S., Langridge, R., Pedley, K., 2010. Surface rupture of the Greendale Fault during the Mw 7.1 Darfield (Canterbury) Earthquake, New Zealand: initial findings. Bull. N. Z. Soc. Earthq. Eng. 43 (4), 236–242.

Rockwell, T.K., Klinger, Y., 2013. Surface rupture and slip distribution of the 1940 Imperial Valley Earthquake, Imperial Fault, Southern California: implications for rupture segmentation and dynamics. Bull. Seismol. Soc. Am. 103 (2A), 629–640. http://dx.doi.org/10.1785/0120120192.

Rockwell, T.K., Lindvall, S., Dawson, T., Langridge, R., Lettis, W., Kinger, Y., 2002. Lateral offsets on surveyed cultural features resulting from the 1999 İzmit and Düzce Earthquakes, Turkey. Bull. Seismol. Soc. Am. 92 (1), 79–94.

Rockwell, T.K., Dawson, T.E., Young Ben-Horin, J., Seitz, G., 2014. A 21 event, 4,000-year history of surface ruptures in the Anza Seismic Gap. San Jacinto Fault and implications for long-term earthquake production on a major plate boundary. Pure Appl. Geophys. http://dx.doi.org/10.1007/s00024-014-0955-z (23pages).

Rosu, A.M., Pierrot-Deseilligny, M., Delorme, A., Binet, R., Klinger, Y., 2014. Measurement of ground displacement from optical satellite image correlation using the free open-source software MicMac. J. Photogramm. Remote. Sens. http://dx.doi.org/10.1016/j.isprsjprs.2014.03.002.

Salisbury, J.B., Rockwell, T.K., Middelton, T.J., Hudnut, K.W., 2012. Lidar and field observations of slip distribution for the most recent surface ruptures along the Central San Jacinto Fault. Bull. Seismol. Soc. Am. 102 (2), 598–619. http://dx.doi.org/10.1785/0120110068.

Salisbury, J.B., Haddad, D.E., Rockwell, T.E., Arrowsmith, J.R., Madugo, C., Zielke, O., Scharer, K., 2014. A validation of meter-scale surface offset measurements from high-resolution topographic data. Bull. Seismol. Soc. Am. (submitted).

Savage, J.C., Lisowski, M., 1995. Interseismic deformation along the San Andreas Fault in Southern California. J. Geophys. Res. 100, 12,703–12,717. http://dx.doi.org/10.1029/95JB01153.

Scharer, K.M., 2013. *New Paleoeismic Data From SoSAFE: Time Dependency and Rupture Patterns on the San Andreas and San Jacinto Faults*, presented at 2013 Annual Meeting. SCEC, Palm Springs, Calif.

Scharer, K.M., Biasi, G.P., Weldon II, R.J., Fumal, T.E., 2010. Quasi-periodic recurrence of large earthquakes on the southern San Andreas Fault. Geology 38 (6), 555–558. http://dx.doi.org/10.1130/G30746.1.

Scharer, K.M., Biasi, G.P., Weldon, R.J., 2011. A reevaluation of the Pallett Creek earthquake chronology based on new AMS radiocarbon dates, San Andreas fault, California. J. Geophys. Res. 116, B12111. http://dx.doi.org/10.1029/2010JB008099.

Scharer, K.M., Salisbury, J.B., Arrowmith, J.R., Rockwell, T.K., 2014a. Southern San Andreas fault evaluation field activity: approaches to measuring small geomorphic offsets—challenges and recommendations for active fault studies. Seismol. Res. Lett. 85 (1), 68–76. http://dx.doi.org/10.1785/0220130108.

Scharer, K., Weldon II, R., Streig, A., Fumal, T., 2014b. Paleoearthquakes at Frazier Mountain, California delimit extent and frequency of past San Andreas fault ruptures along 1857 trace. Geophys. Res. Lett. 41, 4,527–4,534. http://dx.doi.org/10.1002/2014GL060318.

Schmalzle, G., Dixon, T., Malservisi, R., Govers, R., 2006. Strain accumulation across the Carrizo Segment of the San Andreas Fault, California: impact of laterally varying crustal properties. J. Geophys. Res. 111, B05403. http://dx.doi.org/10.1029/2005JB003843.

Scholz, C.H., 1988. The brittle-plastic transition and the depth of seismic faulting. Geol. Rundsch. 77 (1), 319–328.

Schonher, T., Nicholson, S.E., 1989. The Relationship between California Rainfall and ENSO events. Journal of Climate 2, 1258–1269.

Schwartz, D.P., Coppersmith, K.J., 1984. Fault behavior and characteristic earthquakes: examples from the Wasatch and San Andreas Fault Zones. J. Geophys. Res. 89 (B7), 5681–5698.

Schwartz, D.P., Coppersmith, K.J., 1986. Seismic Hazards—New Trends in Analysis Using Geologic Data, in Active Tectonics. National Academy Press, Washington, D.C., pp. 215–230.

Schwartz, D.P., Haeussler, P.J., Seitz, G.G., Dawson, T.E., 2012. Why the 2002 Denali fault rupture propagated onto the Totschunda fault: implications for fault branching and seismic hazards. J. Geophys. Res. 117, B11304. http://dx.doi.org/10.1029/2011JB008918.

Shedlock, K., Tanner, J.G., 1999. Seismic Hazard map of the Western Hemisphere. Ann. Geophys. 42 (6), 1199–1214.

Sherrod, B.L., Brocher, T.M., Weaver, C.S., Bucknam, R.C., Blakely, R.J., Kelsey, H.M., Nelson, A.R., Haugerud, R.A., 2004. Holocene fault scarps near Tacoma, Washington. Geology 32, 9–12. http://dx.doi.org/10.1130/G19914.1.

Sieh, K.E., 1978. Slip along the San Andreas fault associated with the Great 1857 Earthquake. Bull. Seismol. Soc. Am. 68 (5), 1421–1448.

Sieh, K.E., 1981. In: Simpson, D.W., Richards, P.G. (Eds.), Earthquake Prediction, An International Review, Maurice Ewing Set. vol. 4. AGU, Washington, D.C., pp. 181–207.

Sieh, K.E., 1996. The repetition of large-earthquake ruptures. Proc. Natl. Acad. Sci. U. S. A. 93, 3,764–3,771.

Sieh, K.E., Jahns, R.H., 1984. Holocene activity of the San Andreas Fault at Wallace Creek, California. Geol. Soc. Am. Bull. 95, 883–896.

Sieh, K.E., Stuiver, M., Brillinger, D., 1989. A more precise chronology of earthquakes produces by the San Andreas Fault in Southern California. J. Geophys. Res. 94, 603–623.

Sieh, K.E., Jones, L., Hauksson, E., Hudnut, K., Eberhart-Phillips, D., Heaton, T., Hough, S., Hutton, K., Kanamori, H., Lilje, A., Lindvall, S., McGill, S., Mori, J., Rubin, C., Spotila, J., Stock, J., Kie Thio, H., Treiman, J., Wernicke, B., Zachariasen, J., 1993. Near-field investigations of the Landers earthquake sequence. Science 260, 171–176 (April to July 1992).

Stein, S., Wysession, M., 2002. An Introduction to Seismology, Earthquakes, and Earth Structure, 1st edition. Blackwell Publishing Ltd., Oxford, U.K.

Stesky, R.M., Brace, W.F., Riley, D.K., Robin, P.-Y.F., 1974. Friction in faulted rock at high temperature and pressure. Tectonophysics 23, 177–203.

Stirling, M.W., Wesnousky, S.G., Shimazaki, K., 1996. Fault trace complexity, cumulative slip, and the shape of the magnitude–frequency distribution for strike-slip faults: a global survey. Geophys. J. Int. 124, 833–868.

Toda, S., Tsutsumi, H., 2013. Spontaneous reactivation of two, subparallel, inland normal faults during the Mw 6.6 11 April 2011 Iwaki Earthquake triggered by the Mw 9.0 Tohoku-oki, Japan, Earthquake. Bull. Seismol. Soc. Am. 103 (2B), 1,584–1,602.

Toppozada, T.R., Branum, D.M., Reichle, M.S., Hallstrom, C.L., 2002. San Andreas Fault Zone, California: M>= 5.5 Earthquake History. Bull. Seismol. Soc. Am. 92 (7), 2555–2601.

Triggs, W., McLauchlan, P., Hartley, R., Fitzgibbon, A., 1999. *Bundle Adjustment: A Modern Synthesis*, in: Vision Algorithms: Theory and Practice. Springer-Verlag, Corfu, Greece, pp. 298–373.

Tullis, T.E., 2007. Friction of rock at earthquake slip rates. In: Schubert, Gerald (Ed.), Treatise on GeophysicsEarthquake Seismology vol. 4. Elsevier.

Tullis, T.E., Weeks, J.D., 1986. Constitutive behavior and stability of frictional sliding of granite. Pure Appl. Geophys. 124, 10–42.

Wallace, R.E., 1968. Notes on stream channels offset by the San Andreas Fault, Southern Coast Ranges, Caliornia. In: Dickson, W.R., Grantz, A. (Eds.), Prof. of Conf. on Geologic Problems of the San Andreas fault system. Stanford Univ. Publ., Geol. Sci., Univ. Ser. 11, pp. 6–21.

Wallace, R.E., 1991. *The San Andreas Fault System, California*, U.S. Geological Survey. Professional Paper 1515. United States Government Printing Office, Washington D.C.

Ward, S.N., 1997. Dogtails versus rainbows: synthetic earthquake rupture models as an aid in interpreting geological data. Bull. Seismol. Soc. Am. 87, 1,422–1,441.

Wei, S., Fielding, E., Leprince, S., Sladen, A., Avouac, J.-P., Helmberger, D., Hauksson, E., Chu, R., Simons, M., Hudnut, K., Herring, T., Briggs, R., 2011. Superficial simplicity of the 2010 El Mayor–Cucapah Earthquake of Baja California in Mexico. Nat. Geosci. 4 (9), 615–618. http://dx.doi.org/10.1038/ngeo1213.

Weldon II, R.J., McCalpin, J.P., Rockwell, T.K., 1996. Paleoseismology of strike-slip tectonic environments. In: McCalpin, J. (Ed.), Paleoseismology. Academic Press, San Diego, pp. 271–329.

Weldon, R.J., Fumal, T., Biasi, G., 2004. Wrightwood and the earthquake cycle. Geol. Soc. Am. Today 14 (9). http://dx.doi.org/10.1130/1052-5173.

Weldon, R.J., Fumal, T.E., Biasi, G.P., Scharer, K.M., 2005. Past and future earthquakes on the San Andreas Fault. Science 308, 966–967. http://dx.doi.org/10.1126/science.1111707.

Wells, D.L., Coppersmith, K.J., 1994. New empirical relationships among magnitude, rupture length, rupture width, rupture area, and surface displacement. Bull. Seismol. Soc. Am. 84 (4), 974–1,002.

Wesnousky, S.G., 1988. Seismological and structural evolution of strike-slip faults. Nature 335, 340–343.

Wesnousky, S.G., 1994. The Gutenberg–Richter or characteristic earthquake distribution, which is it? Bull. Seismol. Soc. Am. 84 (6), 1,940–1,959.

Wesnousky, S.G., 2006. Predicting the endpoints of earthquake ruptures. Nature 444, 358–360. http://dx.doi.org/10.1038/nature05275.

Westoby, M.J., Brasington, J., Glasser, N.F., Hambrey, M.J., Reynolds, J.M., 2012. 'Structure-from-Motion' photogrammetry: a low-cost, effective tool for geoscience applications. Geomorphology 179, 300–314. http://dx.doi.org/10.1016/j.geomorph.2012.08.021.

Xu, X., Yu, G., Klinger, Y., Tapponnier, P., Van der Woerd, J., 2006. Re-evaluation of surface rupture parameters and faulting segmentation of the 2001 Kunlunshan Earthquake (Mw 7.8), Northern Tbet Plateau, China. J. Geophys. Res. 111, B05316. http://dx.doi.org/10.1029/2004JB003488.

Yokoyama, R., Shirasawa, M., Pike, R.J., 2002. Visualizing topography by openness: a new application of image processing to digital elevation models. Photogramm. Eng. Remote Sens. 68 (3), 257–265.

Zachariesen, J., Sieh, K.E., 1995. The transfer of slip between two en echelon strike-slip faults: a case study from the 1992 Landers Earthquake, Southern California. J. Geophys. Res. 100 (B8), 15,281–15,301.

Zielke, O., Arrowsmith, J.R., 2008. Depth variation of coseismic stress drop explains bimodal earthquake magnitude–frequency distribution. Geophys. Res. Lett. 35, L24301. http://dx.doi.org/10.1029/2008GL036249.

Zielke, O., Arrowsmith, J.R., Grant Ludwig, L., Akçiz, S.O., 2010. Slip in the 1857 and earlier large earthquakes along the Carrizo Plain, San Andreas Fault. Science 327, 1,119–1,122. http://dx.doi.org/10.1126/science.1182781.

Zielke, O., Arrowsmith, J.R., 2012. LaDiCaoz and LiDARimager–MATLAB GUIs for LiDAR data handling and lateral displacement measurement. Geosphere 8 (1), 206–221. http://dx.doi.org/10.1130/GES00686.1.

Zielke, O., Arrowsmith, J.R., Grant Ludwig, L., Akçiz, S.O., 2012. High-resolution topography-derived offsets along the 1857 Fort Tejon Earthquake Rupture Trace, San Andreas Fault. Bull. Seismol. Soc. Am. 102 (3), 1,135–1,154. http://dx.doi.org/10.1785/0120110230.